

University of Groningen

Cool dust and gas in the Small Magellanic Cloud

Stanimirovic, S; Staveley-Smith, L; van der Hulst, JM; Bontekoe, TR; Kester, DJM; Jones, PA

Published in:
Monthly Notices of the Royal Astronomical Society

DOI:
[10.1046/j.1365-8711.2000.03480.x](https://doi.org/10.1046/j.1365-8711.2000.03480.x)

IMPORTANT NOTE: You are advised to consult the publisher's version (publisher's PDF) if you wish to cite from it. Please check the document version below.

Document Version
Publisher's PDF, also known as Version of record

Publication date:
2000

[Link to publication in University of Groningen/UMCG research database](#)

Citation for published version (APA):

Stanimirovic, S., Staveley-Smith, L., van der Hulst, JM., Bontekoe, TR., Kester, DJM., & Jones, PA. (2000). Cool dust and gas in the Small Magellanic Cloud. *Monthly Notices of the Royal Astronomical Society*, 315(4), 791-807. <https://doi.org/10.1046/j.1365-8711.2000.03480.x>

Copyright

Other than for strictly personal use, it is not permitted to download or to forward/distribute the text or part of it without the consent of the author(s) and/or copyright holder(s), unless the work is under an open content license (like Creative Commons).

Take-down policy

If you believe that this document breaches copyright please contact us providing details, and we will remove access to the work immediately and investigate your claim.

Downloaded from the University of Groningen/UMCG research database (Pure): <http://www.rug.nl/research/portal>. For technical reasons the number of authors shown on this cover page is limited to 10 maximum.

Cool dust and gas in the Small Magellanic Cloud

S. Stanimirovic,^{1,2}★† L. Staveley-Smith,² J. M. van der Hulst,³ Tj. R. Bontekoe,^{4,5}
D. J. M. Kester⁶ and P. A. Jones¹

¹University of Western Sydney Nepean, PO Box 10, Kingswood, NSW 2747, Australia

²Australia Telescope National Facility, CSIRO, PO Box 76, Epping, NSW 2121, Australia

³Kapteyn Astronomical Institute, Postbus 800, NL-9700 AV Groningen, the Netherlands

⁴Bontekoe Data Consultancy, Herengracht 2 B, 2312 LD Leiden, the Netherlands

⁵Astronomical Institute 'Anton Pannekoek', University of Amsterdam, Kruislaan 403, 1098 SJ Amsterdam, the Netherlands

⁶Laboratorium voor Ruimteonderzoek, SRON, PO Box 800, 9700 AV Groningen, the Netherlands

Accepted 2000 February 7. Received 2000 January 24; in original form 1999 October 8

ABSTRACT

We present high-angular-resolution, far-infrared images of the Small Magellanic Cloud (SMC). The images were reconstructed from data obtained with the *Infrared Astronomical Satellite* (IRAS), using the Pyramid Maximum Entropy algorithm. The angular resolutions of the images are 1 arcmin at 12, 25 and 60 μm , and 1.7 arcmin at 100 μm , which provides an excellent complement to the recent neutral hydrogen (HI) survey from the Australia Telescope Compact Array, which has a resolution of 1.6 arcmin. We use the 60- and 100- μm data, together with a standard dust model, to derive a temperature map and a dust column density distribution. Dust temperatures range from 23 to 45 K, which is, on average, warmer than for the Galaxy, although there is a deficit of warm, very small dust grains in the SMC. The total amount of cool dust in the SMC is $1.8_{-0.2}^{+1.3} \times 10^4 M_{\odot}$. There is a significant variation of the observed dust-to-gas ratio across the SMC. This may be caused by corresponding variations in metallicity, but this explanation is not supported by the limited available data in the literature. Alternatively, there may be a large amount of molecular hydrogen (H_2) in the SMC, $\sim 8 \times 10^8 M_{\odot}$, and/or a large amount ($\sim 10^6 M_{\odot}$) of cold dust (≤ 15 K) not seen by IRAS or COBE/DIRBE. The average dust-to-atomic gas ratio is, by mass, 8.2×10^{-5} , which is a factor of ~ 30 below the Galactic value. The spatial power spectrum of the dust column density image can be approximated by $P_d(k) \propto k^{-3.1}$, which shows that, as with the HI power spectrum, there is no preferred scale size for dust clouds. A spatial coherence analysis shows that, over a wide range of spatial scales (≥ 50 pc), HI and dust are well correlated (> 60 per cent).

Key words: ISM: clouds – dust, extinction – Magellanic Clouds – infrared: galaxies.

1 INTRODUCTION

The Small Magellanic Cloud (SMC) is the third member of an interacting threesome of galaxies (Murai & Fujimoto 1980), the other members of which are the Large Magellanic Cloud (LMC) and the Galaxy. Being of the lowest mass, the SMC is the most disrupted by the apparently gravitational nature of the interactions (Putman et al. 1998), and its large-scale morphology is complex and not fully understood. However, the SMC is extremely rich in neutral atomic gas (Staveley-Smith et al. 1998), and is the site of several giant H II regions and numerous molecular clouds (Rubio, Lequeux & Boulanger 1993). It is of interest as an extremely

nearby example of star formation in an almost primordial medium with low heavy-element abundance (Sauvage & Vigroux 1991) and high UV-bright interstellar radiation field (Lequeux 1989). Its proximity makes it possible to obtain data on size scales of a few parsecs and less, but it is also far enough away that all objects are at much the same distance, which is relatively well-determined at ~ 60 kpc¹ (Westerlund 1991).

Being a gas-rich system, the most important component of the cool ISM in the SMC is neutral hydrogen (HI), which we have recently studied using aperture synthesis mosaiking (Staveley-Smith et al. 1997; Stanimirovic et al. 1999). However, there are other important tracers of the cool ISM such as ionized carbon, which provides an important cooling line at 158 μm (Kulkarni & Heiles 1989), and dust, which is a source of coupling between

★ E-mail: sstanimi@naic.edu

† Present address: Arecibo Observatory, HC 3 Box 53995, Arecibo, Puerto Rico 00612.

¹Throughout this paper we assume a distance to the SMC of 60 kpc.

neutral and ionized gas, as well as a catalyst for the creation of molecules in dense regions (Dyson & Williams 1997).

A study of dust and gas in the SMC can help us to address various astrophysical questions, such as the following.

(i) How does the morphology and the phase-mix of the ISM in a low-metallicity, less-evolved galaxy differ from that in a well-evolved galaxy, such as our Galaxy?

(ii) What triggers star formation? Is there a threshold density of gas necessary for the star burst (Knapp 1990)? What is the aftermath of star formation on the ISM?

(iii) Once initiated, by what detailed mechanisms does star formation propagate in a galaxy where density waves are unimportant?

(iv) How does metallicity evolve with time (Knapp 1990)?

(v) Which physical processes cause the starburst-like dust properties of the SMC? Are they dependent on metallicity and/or star formation, and how (Gordon & Clayton 1998)?

In this paper we concentrate mainly on the dust properties of the SMC and its relation with the cool gas in the ISM. Early studies of the dust properties and the dust-to-gas ratio, undertaken with ground-based instruments (Koorneef 1982, 1984; Bouchet et al. 1985; Koorneef & Israel 1985; Israel & Koorneef 1988; Lequeux 1989; Martin, Maurice & Lequeux 1989), were limited to the brightest objects in the SMC and covered a negligible fraction of the area of the SMC (Schwering & Israel 1989). The advent of the infrared (IR) all-sky survey by the *Infrared*

Astronomical Satellite (IRAS) resulted in the first complete IR survey of the SMC, which produced a list of point sources (*IRAS* Point Source Catalog 1988, hereafter *IRAS-PSC*) and a series of maps produced from Pointed Observations (POs) (Schwering 1988; Schwering & Israel 1989). While having better resolution, at the time, than the old H I images from the Parkes telescope, these maps compare poorly with the 1.6-arcmin resolution from the Australia Telescope Compact Array (ATCA) survey (Stanimirovic et al. 1999). However, the intrinsic resolution of the *IRAS* telescope optics is 1 arcmin at 60- μm and 1.7 arcmin at 100 μm . By combining several scans at different position angles, it is possible to reconstruct reliable images with a resolution close to the original diffraction limit, and therefore closer to the H I studies. This has been done for many individual fields using the IPAC HiRes program, and has been done for the Galactic plane (Cao et al. 1997). Methods are discussed by Rice (1993) and Bontekoe, Koper & Kester (1994).

In Section 2 of this paper we describe selection and processing of the *IRAS* survey and PO data, the IR morphology of the SMC, comparison with other *IRAS* and *COBE/DIRBE* data, and details of the assumed dust model. In Section 3 the dust temperature, dust column density distribution, the total dust mass and its uncertainty are derived and discussed. We derive the dust-to-gas ratio in Section 4, discuss possible reasons for its spatial variation, and compare our results with previous studies. Section 5 investigates spatial power spectra of 60- and 100- μm bands, and dust and H I column density

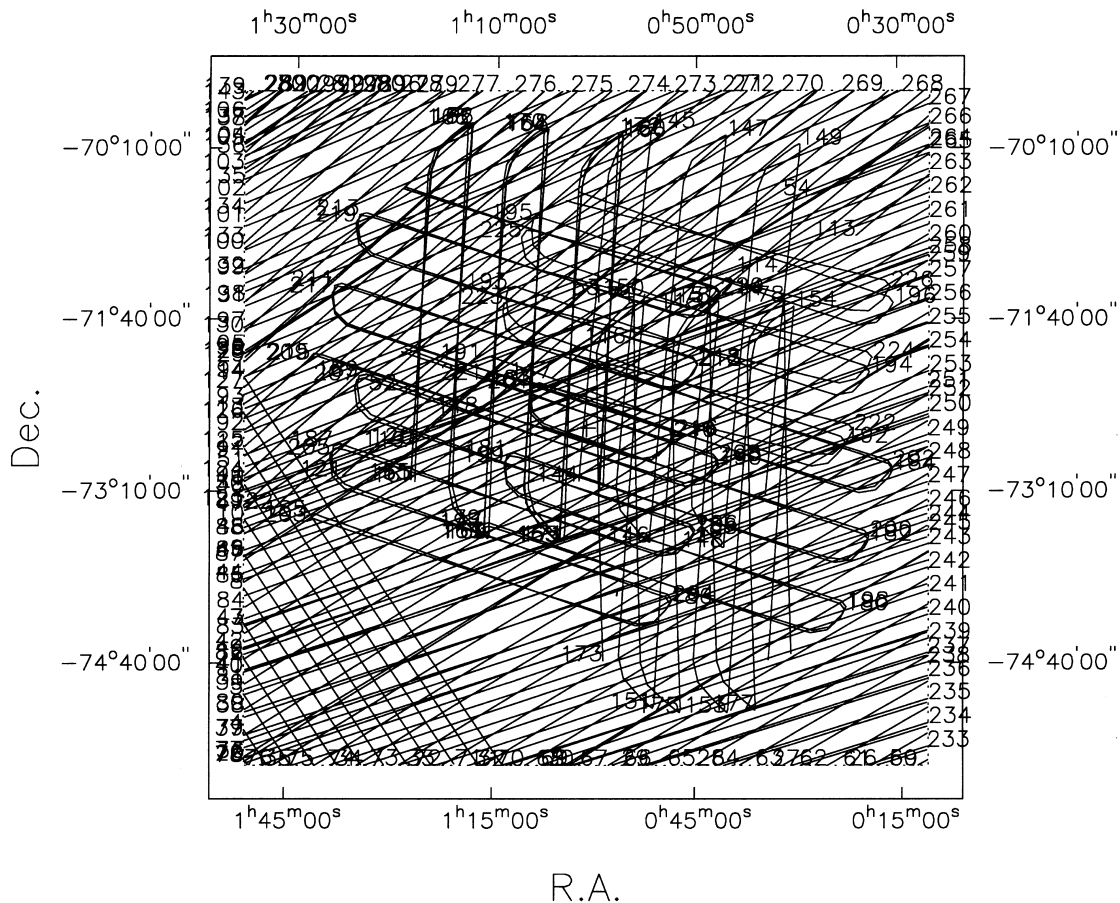


Figure 1. The *IRAS* scan pattern of the SMC (J2000). Three sets of scans of survey data are present: HCON-1 and HCON-2 (see *IRAS* Catalogs and Atlases Explanatory Supplement, Beichman et al. 1985), which are almost parallel and run from south-east to north-west, and HCON-3, perpendicular to both but covering just a small area at the south-east. 14 DMP Pointed Observations (Young et al. 1985) covering the central region of the SMC in various directions are also shown.

images. We discuss further the spatial correlation between dust and HI column density, using the spatial coherency spectrum.

2 DATA AND RESULTS

2.1 HIRAS data

2.1.1 Data origin and processing

The HIRAS program (Bontekoe et al. 1994) was used to produce the high-resolution IR maps of the SMC from the *IRAS* all-sky survey data in three sets of scans in conjunction with 14 Pointed Observations (POs). Note that HIRAS should not be confused with HiRes, which uses a maximum-correlation technique (Aumann, Fowler & Melnyk 1990). The scan pattern of the data used in this paper is shown in Fig. 1. The addition of the POs nearly doubled the amount of data, but the main reason for their inclusion is the fact that the SMC survey data are taken predominantly in one direction over the map (i.e., from south-east to north-west), while the POs add scans with various other angles. The quality of the individual images has been greatly improved by the inclusion of

POs. The dust temperature image in particular was of unacceptable quality when made from survey data alone.

In the calibration procedure, data samples from detectors known to be noisy were discarded and glitches in the data (due to cosmic ray hits) were identified and removed. The zodiacal emission model was then subtracted from all data scans individually. To provide the calibration consistency between different scans, an iterative ‘de-stripping’ algorithm was applied to take account of the baseline differences between the scans. For more details on *IRAS* data calibration and pre-processing, see Bontekoe et al. (1994), Kester & Bontekoe (1994) and Assendorp et al. (1995). After subtraction of the zodiacal emission model and subsequent ‘de-stripping’, the zero-point of the data is arbitrary. Since there is no clear selection criterion, a (personal) judgment must be made based on the distribution of all data values. One possibility is to take the fiducial zero-point such that typically 3–5 per cent of all the data become negative. An alternative, used here, is to determine the half-width at half-maximum of the distribution of data values, and subtract this half-width from the value of the mode of the distribution (i.e., where the maximum occurs). Both

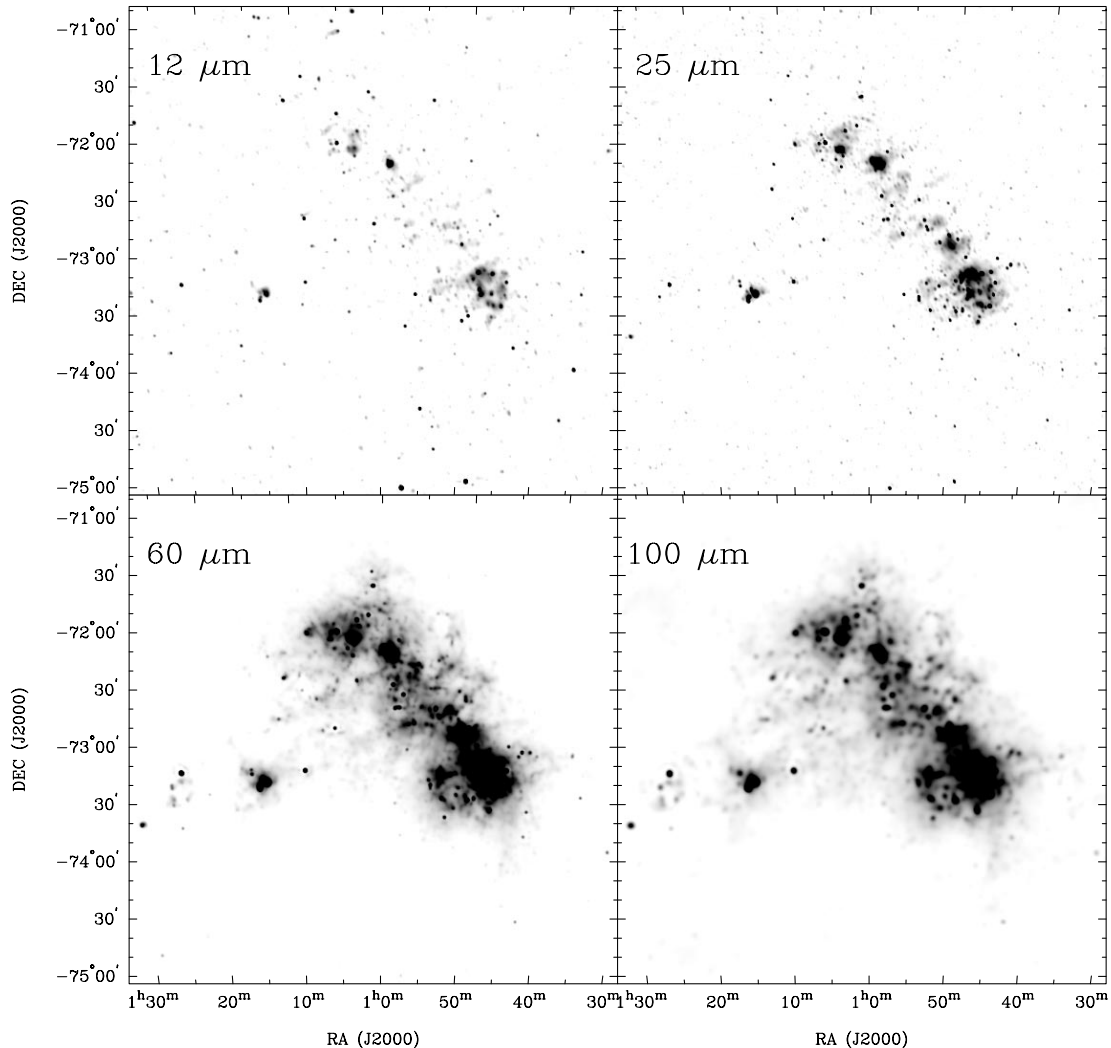


Figure 2. The high-resolution PME *IRAS* images of the SMC at 12, 25, 60 and 100 μm . The grey-scale intensity range is: 0.2 to 1.2, 0.2 to 1.9, 0.6 to 13 and 0.6 to 27 MJy sr^{-1} , respectively, with a linear transfer function. The 12-, 25- and 60- μm images have a resolution of ~ 1 arcmin, while the 100- μm image has a resolution of ~ 1.7 arcmin.

Table 1. Comparison of integrated IR flux densities of the SMC from different surveys. The area covered is $\sim 6.25 \text{ deg}^2$.

| Band (μm) | DIRBE ^a (Jy) | DIRBE + ISSA ^b (Jy) | HIRAS ^c (Jy) | IRAS (POS) ^d (Jy) |
|---------------------------|----------------------------|-----------------------------------|----------------------------|---------------------------------|
| 1.25 | 510 ± 25 | – | – | – |
| 2.2 | 400 ± 37 | – | – | – |
| 3.5 | 220 ± 31 | – | – | – |
| 4.9 | 110 ± 43 | – | – | – |
| 12 | 80 ± 30 | – | 105 ± 30 | 147 ± 26 |
| 25 | 460 ± 180 | – | 310 ± 170 | 385 ± 56 |
| 60 | 8450 ± 370 | – | 6700 ± 1060 | 7170 ± 957 |
| 100 | 15800 ± 2720 | 15000 ± 2610 | 13600 ± 1930 | 13900 ± 1810 |
| 140 | 14000 ± 5600 | – | – | – |
| 240 | 9600 ± 4400 | – | – | – |

^a *COBE*/DIRBE data in public domain^b from Schlegel et al. (1998)^c this paper^d from Schwing (1988)

methods yield the best possible *IRAS* images, which, however, still require some careful post-processing flat-fielding.

Bayesian data analysis (based on Bayesian probability theory), employed in the *HIRAS* program, requires an uncertainty for every measured quantity (see Sivia 1996 for an excellent tutorial). This property is used extensively to incorporate known instrumental effects as an extra contribution in the uncertainty of the input data. These instrumental effects include the lossy data compression scheme on board of the satellite, the detector memory effects, and glitches due to cosmic ray hits. Correction for truncation effects in the data digitization is also made. Note that a number of the above calibration steps are performed by comparing the data against fiducial data sampled from a low-resolution map. We have found that a single pre-processing pass of the calibration steps is not sufficient. Therefore, after every convergence of our *HIRAS* program, some further refinements in the calibration can be made against a high-resolution map. Typically, three to four iterations are needed until no further improvements seem possible.

The *HIRAS* program uses the Pyramid Maximum Entropy (PME) method, an application of the maximum entropy package MemSys5 (Gull & Skilling 1991), to reconstruct reliable images at a resolution approaching the diffraction limit of the *IRAS* telescope. In the PME algorithm the image is reconstructed in a number of channel images, all computed in parallel, containing respectively 1 by 1 pixels, 2 by 2 pixels, 4 by 4 pixels, 8 by 8 pixels, etc. up to the final pixel number (here 1024 by 1024 pixels). The final image is constructed from the channel images in three steps. First, each channel image is regridded into pixels of the desired map (here 1024 by 1024) and, second, each regridded image is blurred with a Gaussian profile having a width (standard deviation) of 1.0 times the pixel size in ‘its’ channel image. Third, the regridded and blurred images are added, pixel by pixel. The final image is thus the sum of several images blurred with Gaussian of different widths. This is a very effective method of reconstructing many spatial scalelengths into a single image, because the entropy acts as a ‘filter’. The entropy is the sum of entropies of the channel images, irrespective of the sizes of the pixels. Maximizing this sum ensures that large-scale structure is preferentially reconstructed in a channel image with large pixels, because this is ‘cheaper in entropy’.

The resulting images of the SMC have a resolution of ~ 1 arcmin for the 12-, 25- and 60- μm data, and ~ 1.7 arcmin for the 100- μm data. As the actual resolution and the dynamic range depend on the local sampling pattern (and source

brightness), they vary slightly across the maps. To obtain true intensities from the in-band ones, we have applied colour corrections from the *IRAS* Catalogs and Atlases Explanatory Supplement (Beichman et al. 1985). After fitting the observed integrated spectrum with a power law, the correction factors are derived to be 0.93, 0.92, 0.99, 1.00 for 12, 25, 60 and 100 μm , respectively. All images were flat-fielded to remove the residual background.

2.1.2 IR morphology

The resulting high-resolution *IRAS* images of the SMC in all four bands are shown in Fig. 2. The *HIRAS* data resemble the IR distribution across the SMC found in previous studies, but for the first time contain information on scales as small as ~ 1 arcmin (for 12, 25 and 60 μm) and ~ 1.7 arcmin (for 100 μm). While the 12- and 25- μm images trace mainly hot H II regions and foreground stars with little diffuse IR emission, the 60- and 100- μm data show a lot of diffuse emission with a wealth of filamentary structure. Some residual, low-level stripes (below the 3σ noise level) are still visible in the 12- and 25- μm images, due to the scan pattern. The astrometric and photometric agreement of point sources with the *IRAS*-PSC are on average good, although PME fluxes are 10–20 per cent higher (for more detail on image quality estimate and comparison, see Bontekoe et al. 1994). As the SMC has a high ecliptic latitude, the contribution of the zodiacal emission is not significant, unlike in the Galaxy where 12-, 25- and 60- μm bands are severely contaminated (Schlegel, Finkbeiner & Davis 1998). This, together with the mainly flat and featureless Galactic background around the SMC, enables good reconstruction of the diffuse IR emission.

2.1.3 Comparison with other IR observations

In Table 1 we show a comparison of the integrated flux densities from our data with IR data from three other sources.

(i) *COBE*/DIRBE maps² for 1.25–240 μm , with a resolution of 0.7° . We have applied colour corrections from the *COBE*/DIRBE Explanatory Supplement (Hauser et al. 1998) and applied a

² The *COBE* data sets were developed by the NASA Goddard Space Flight Center under the guidance of the *COBE* Science Working Group, and were provided by the NSSDC.

foreground correction, but have not applied any specific zodiacal emission corrections.

(ii) A composite of *COBE*/DIRBE and *IRAS*/ISSA maps at $100\ \mu\text{m}$, corrected for the zodiacal background and colour, with 6-arcmin resolution (from Schlegel et al. 1998). We further applied a correction to remove extended foreground Galactic emission.

(iii) *IRAS* non-survey ‘Pointed Observation’ images, corrected for both zodiacal emission and colour, with 8-arcmin resolution (from Schwering 1988).

Flux densities in Table 1 were obtained by summing the maps over an area of $6.25\ \text{deg}^2$ which contains the optical bar and the Eastern Wing (a region seen eastwards of RA $01^{\text{h}}\ 10^{\text{m}}$). Error estimates are dominated by the background corrections and uncertainties in the absolute flux density scale.

Except for the 4.9-, 12- and $25\text{-}\mu\text{m}$ *COBE*/DIRBE data, where the zodiacal emission peaks and the SMC emission is at a minimum, flux densities from all data sources seem to be comparable within 10–20 per cent uncertainty. We find very good agreement between HIRAS and *IRAS* fluxes. Surprisingly, integrated flux densities measured by *COBE*/DIRBE for 60 and $100\ \mu\text{m}$ [from both (i) and (ii)] are higher than HIRAS or *IRAS* fluxes by about 10–20 per cent, whereas the *IRAS* Sky Survey Atlas Explanatory Supplement (Wheelock et al. 1994) gives a linear transformation between *IRAS* and DIRBE data, in which the *IRAS* brightnesses are 13 and 28 per cent higher than DIRBE brightnesses at 60 and $100\ \mu\text{m}$, respectively. A possible reason why we measure higher *COBE*/DIRBE integrated flux densities for the SMC could be a position- or resolution-dependent brightness transformation between *IRAS* and DIRBE data.

The integrated HIRAS spectrum of the SMC is shown in Fig. 3 and compared with data from the above three data sources. Flux densities for 0.4 and $0.5\ \mu\text{m}$ were estimated from the blue and visual apparent magnitudes of the SMC, obtained from the Third Reference Catalogue of Bright Galaxies (de Vaucouleurs et al. 1991, hereafter RC 3), and they seem to be consistent (although

they do not overlap) with *COBE*/DIRBE data. The stellar radiation is responsible for the $\lambda \lesssim 4\ \mu\text{m}$ part of the spectrum. The overall spectrum peaks at $\sim 100\ \mu\text{m}$ (although in νf_ν units the spectrum peaks at $\sim 1\ \mu\text{m}$). Unlike Galactic IR emission which shows a secondary peak around $\lambda \sim 10\ \mu\text{m}$ (Cox & Mezger 1989), the SMC IR spectrum has a local minimum at $\lambda \sim 12\ \mu\text{m}$. Therefore the excess near-IR and mid-IR emission is not prominent, indicating that PAH molecules, responsible for IR emission at these wavelengths, play a less important role in the SMC than in the Galaxy.

Quasi-blackbody spectra, $\kappa_\nu B_\nu(T_d)$, for dust mass absorption coefficient $\kappa_\nu \propto \nu^{2.0}$ and a range of dust temperatures $T_d = 30, 25, 20$ and $15\ \text{K}$, are overlaid in Fig. 3. The far-IR part of the spectrum ($\lambda \gtrsim 45\ \mu\text{m}$) seems to be reasonably well modelled with some combination of the quasi-blackbody curves for temperature range 15–30 K. This means that large dust grains are predominantly responsible for IR emission at $\lambda \gtrsim 45\ \mu\text{m}$. The discrepancy for $\lambda < 45\ \mu\text{m}$ probably corresponds to the presence of some very small grains (VSGs).

2.1.4 SMC dust model and assumptions

The dust model we assume is based on studies by Mathis, Rumpl & Nordsieck (1977), Draine & Anderson (1985), Dwek et al. (1997), Li & Greenberg (1997) and Rodrigues et al. (1997), and consists of:

- (i) large silicate and carbonaceous (graphite or amorphous carbon) grains, with sizes $a \gtrsim 0.05\ \mu\text{m}$ (so-called normal grains);
- (ii) very small carbonaceous grains (VSGs), with sizes $a \lesssim 0.005\ \mu\text{m}$, and
- (iii) PAH molecules.

While the early dust models in general considered bare silicate and carbonaceous grains, the most recent models are more complex and consider silicate cores coated by the carbonaceous mantle or composite dust grains (collections of very small dust

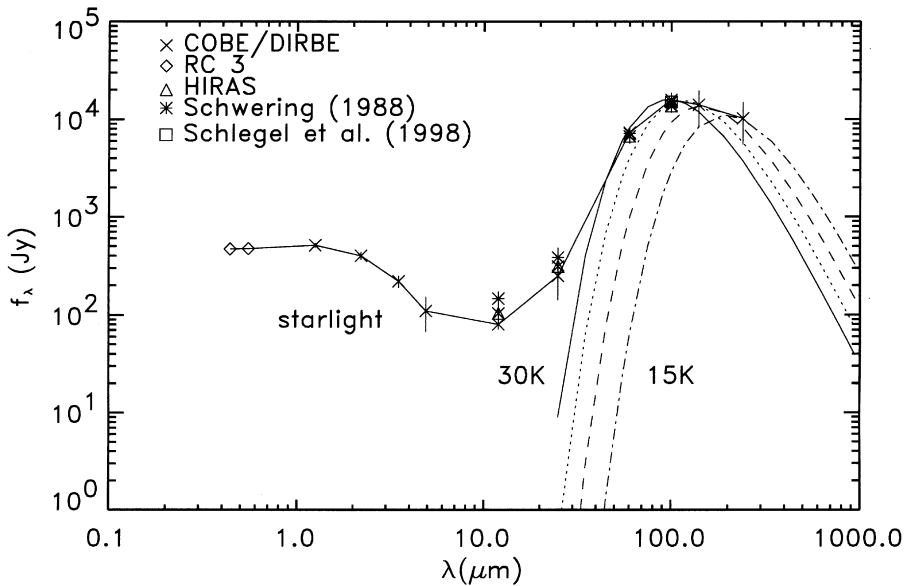


Figure 3. The integrated IR spectrum of the SMC from five different data sources: *COBE*/DIRBE data (crosses), the Third Reference Catalogue of Bright Galaxies (de Vaucouleurs et al. 1991) (diamonds), HIRAS data (triangles), Schwering (1988) (asterisks) and Schlegel et al. (1998) (square). The quasi-blackbody spectra for temperature $T_d = 30\ \text{K}$ (solid line), $25\ \text{K}$ (dotted line), $20\ \text{K}$ (dashed line) and $15\ \text{K}$ (dot-dashed line), and assumed dust mass absorption coefficient $\kappa_\nu = 41(\nu/c)^{2.0}\ \text{cm}^2\ \text{g}^{-1}$, are overlaid.

particles loosely attached to one another) (see Li & Greenberg 1997 for a review). The very recent work by Zubko (1999) suggests a dust model for the SMC which consists of a mixture of the silicate core–organic refractory mantle and composite grains, and also includes silicon nanoparticles. However, this model has been fitted to the observational data only for the star AzV 398, situated in the SMC bar.

The main constraint for the abundances of dust grains comes from the SMC extinction curve. Compared to the Galaxy, the SMC has a much straighter, almost linear, extinction curve with (a) a weaker $\sim 0.2\text{-}\mu\text{m}$ bump, and (b) a stronger far-ultraviolet (FUV) rise (Lequeux 1989; Sauvage & Vigroux 1991; Gordon & Clayton 1998). Although the carrier of the $0.2\text{-}\mu\text{m}$ bump is still uncertain, it is generally ascribed to the VSGs (Li & Greenberg 1997; Rodrigues et al. 1997). Hence (a) implies an absence of VSGs particularly responsible for the $0.2\text{-}\mu\text{m}$ bump. However, a significant abundance of VSGs, in general, may still be present in the SMC, as suggested by the integrated IR spectrum for $\lambda < 45\ \mu\text{m}$. As the FUV extinction originates from PAH molecules, (b) suggests that the SMC is overabundant in PAHs, which is in contradiction to the low integrated $12\text{-}\mu\text{m}$ emission (see Table 1) produced mainly by PAHs. Rodrigues et al. find evidence that the increase of FUV extinction is associated with regions in the SMC protected from the interstellar radiation field (ISRF) (such as molecular clouds). In general, it seems that PAH molecules are not very abundant in the SMC.

Most of the IR emission of the SMC, for $\lambda > 45\ \mu\text{m}$, seems to arise from large grains [component (i)]. These grains are in thermal equilibrium with the ISRF, and radiate as quasi-blackbody emitters within a narrow temperature range (Dwek et al. 1997).

We assume that FIR emission is optically thin, and that radiation is isotropic. Along each line of sight, therefore, the IR intensity I_ν is an integral over all dust temperatures:

$$I_\nu = \int_T \rho_T \kappa_\nu B_\nu(T) dT, \quad (1)$$

where ρ_T is the mass density of a dust component at temperature T , and κ_ν is the mass absorption coefficient (opacity). The mass absorption coefficient is given by

$$\kappa_\nu = \kappa_{100\mu\text{m}} (\lambda/100\ \mu\text{m})^{-n}, \quad (2)$$

with n varying between 2.0 for graphite, 1.5 for silicate and 1.0 for amorphous carbon. We assume $\kappa_{100\mu\text{m}} = 41\ \text{cm}^2\ \text{g}^{-1}$ and adopt $n = 2.0$ (Reach et al. 1995; Schlegel et al. 1998) in this paper.

2.2 H I data

The H I data are from a combination of Parkes spectral-line observations with an ATCA aperture synthesis mosaic of the SMC (Stanimirovic et al. 1999). The spatial resolution is 98 arcsec, and the velocity resolution is $1.65\ \text{km s}^{-1}$. The area covered is RA $00^{\text{h}}30^{\text{m}}$ to $01^{\text{h}}30^{\text{m}}$ and Dec. -71° to -75° (J2000), over a velocity range of 90 to $215\ \text{km s}^{-1}$. Fig. 4 shows the integrated column-density image. The total estimated mass of the H I, after correction for self-absorption, is $4.2 \times 10^8 M_\odot$.

3 DUST TEMPERATURE DISTRIBUTION

The integrated IR spectrum in Fig. 3 and the discussion in Section

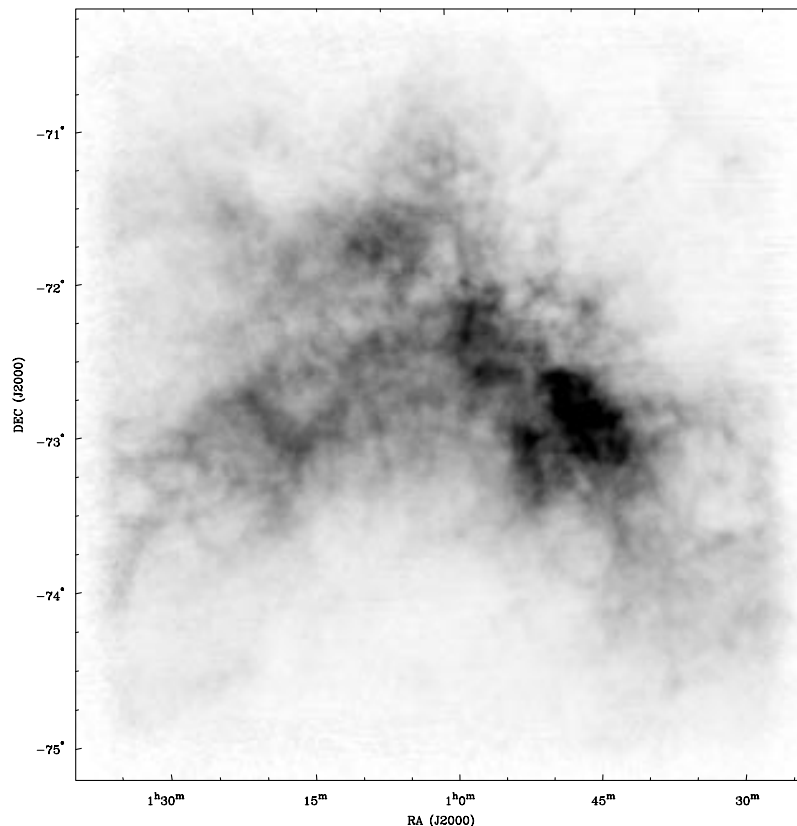


Figure 4. An H I column-density image of the SMC. The grey-scale intensity range is 0 to 1.03×10^{22} atoms cm^{-2} , with a linear transfer function. The maximum H I column density, 1.43×10^{22} atoms cm^{-2} , is at position RA $00^{\text{h}}47^{\text{m}}33^{\text{s}}$, Dec. $-73^{\circ}05'26''$ (J2000).

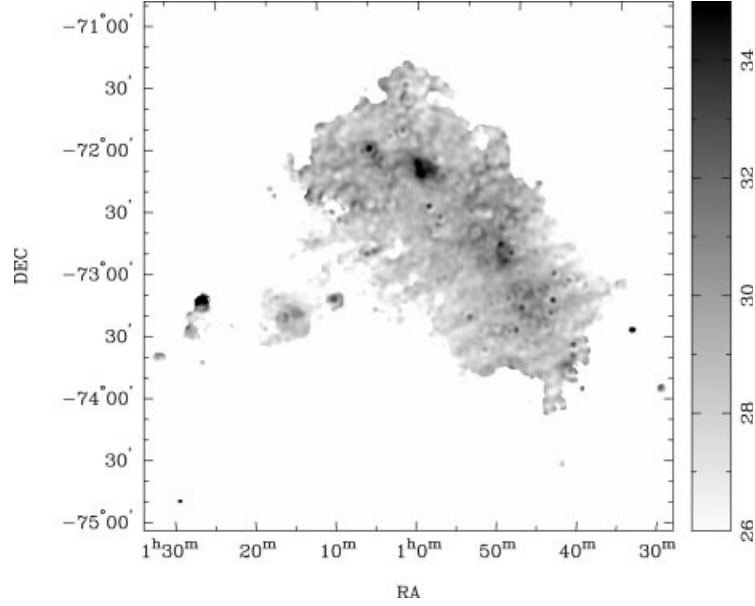


Figure 5. The dust temperature image of the SMC derived from the 60- to 100- μm ratio map. The grey-scale intensity range is 26 to 35 K, with a linear transfer function. The maximum temperature, 45 K, is at position RA 01^h24^m42^s, Dec. -73°11'45" (J2000), which corresponds to N88 (Davies, Elliot & Meaburn 1976).

2.1.4 indicate that normal grains are the most abundant type of dust grains in the SMC. They emit as quasi-blackbodies at $\lambda \gtrsim 60 \mu\text{m}$ within a narrow temperature range. Therefore, under the simplification that along each line of sight only one temperature component is present, the ratio of two spectral points of a quasi-blackbody (I_ν) is recursively related to dust temperature T_d by

$$T_d = \frac{h(\nu_1 - \nu_2)}{k \ln \left[\left(\frac{\nu_1}{\nu_2} \right)^{3+n} \left(\frac{I_{\nu_2}}{I_{\nu_1}} \right) + C_T \right]}, \quad (3)$$

with h and k being Planck's and Boltzmann's constants respectively, n being exponent of the absorption coefficient ($n = 2.0$), and C_T being a temperature-dependent correction factor:

$$C_T = \left[1 - \left(\frac{\nu_1}{\nu_2} \right)^{3+n} \left(\frac{I_{\nu_2}}{I_{nu_1}} \right) \right] \exp \left(\frac{-h\nu_2}{kT_d} \right) \quad (4)$$

(Schwering 1988). However, Schwering shows that using $C_T = 0$ at the 60- and 100- μm bands introduces an error of only 1 K in dust temperature determinations, if $T_d < 45$ K.

To match the point spread functions of 60- and 100- μm images, both images were smoothed to 2.3-arcmin resolution, and the 60-to-100 μm ratio image was derived. Further, applying equation (3), with the assumption that $C_T = 0$, and with a 4σ flux cut-off (to stop noise from propagating), we derive the dust temperature image.

The resultant dust temperature image is shown in Fig. 5. The temperatures vary from 45 K close to H II regions in the optical bar and the Eastern Wing (e.g., N88), dropping to 23 K at the outskirts of the SMC. To compare with the previous results of Schwering (1988), we identify three different temperature regimes in Fig. 5:

(i) $23 < T_d < 29$ K – corresponds to diffuse emission originating from dust heated by the ISRF and covers ~ 54 per cent of the area;

(ii) $29 < T_d < 31$ K – corresponds to the hot diffuse emission

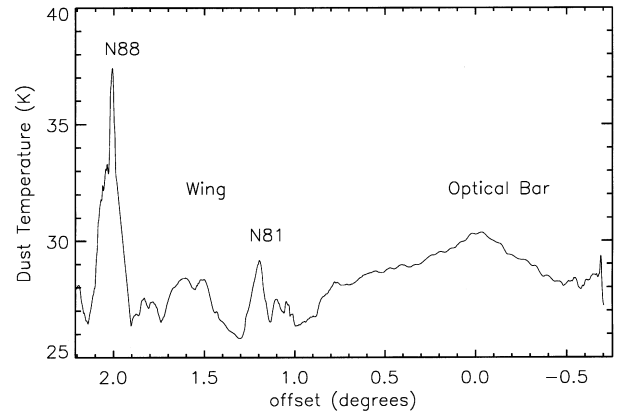


Figure 6. The dust temperature integrated along the optical major axis (at position angle of 40°) and plotted as a function of distance (in degrees) from RA 00^h52^m, Dec. -73°00' (J2000) along the minor optical axis, starting from south-east.

in the environment of prominent H II regions and covers ~ 39 per cent of the area;

(iii) $31 < T_d < 45$ K – corresponds to discrete hot H II regions and covers ~ 7 per cent of the area shown in Fig. 5.

Because of our greater resolution, the overall temperature range we find is greater than that measured by Schwering (1988). Surprisingly, though, we find that the diffuse dust component (i) is much more extensive than the negligible figure suggested by Schwering.

Fig. 6 shows the dust temperature, integrated along the optical major axis (position angle 40°), as a function of distance along the minor optical axis. The optical bar of the SMC, the Eastern Wing and H II regions N88 and N81 are very prominent. The decrease of the dust temperature towards the edges of the optical bar and Eastern Wing (noted above) is now prominent. This is unlike the case for the Galaxy (Sodroski et al. 1994), and probably reflects

the expected decrease of the ISRF away from regions of high stellar density in the SMC. In the Galaxy, emission at 60- μm appears to have a component due to very small dust grains which are not in thermal equilibrium. In the SMC, this component appears to be less significant.

For the Galaxy, Sodroski et al. (1994) find that 60–75 per cent of the far-IR luminosity (at 140 and 240 μm) arises from cold (~ 17 –22 K) dust associated with diffuse H I clouds, 15–30 per cent from cold (~ 19 K) dust associated with molecular clouds, and less than 10 per cent from warm (~ 29 K) dust in extended H II regions. These temperature ranges are somewhat lower than we find in the SMC, suggesting that the SMC has a stronger ISRF possibly due to lower metallicity and higher star formation rate. Schlegel et al. (1998) also find, from 100- and 240- μm full-sky data, that the Galactic dust temperature is lower than that in the SMC, varying between 17 and 21 K.

3.1 Dust mass column density

For a homogeneous object, in the optically thin regime ($\tau_\nu \ll 1$) the dust mass column densities (per unit solid angle) can be calculated from

$$N_d = \frac{I_\nu}{\kappa_\nu B_\nu(T_d)} \frac{1}{\Delta\Omega}, \quad (5)$$

where $\Delta\Omega$ is a solid angle corresponding to an area of 1 cm^2 at the distance of the SMC (Schwering 1988). The slow local variation of the dust temperature enables us to use the dust temperature image, with 2.3-arcmin resolution, in conjunction with a 100- μm

intensity image having 1.7-arcmin resolution. Therefore the resolution of the derived dust mass column density image is 1.7 arcmin. The distribution of the dust column density across the SMC is shown in Fig. 7. This map shows a wealth of small-scale structure, with a variety of filamentary and shell-like features in the optical bar and towards the edges. The column densities range from 0 to $2.1 \times 10^8 \text{ M}_\odot \text{ sr}^{-1}$, or from 0 to 9.4×10^8 dust particles cm^{-2} (where a conversion factor from $\text{M}_\odot \text{ sr}^{-1}$ to dust particles cm^{-2} is equal to 4.45 for the mass of an average grain of $1.3 \times 10^{-17} \text{ kg}$ taken from Schwering 1988). The highest values correspond to H II regions in the optical bar and Eastern Wing.

Equation (5) shows that the derived value for N_d depends strongly on T_d . For the same value of I_ν , a decrease of T_d from 31 to 23 K would increase N_d by a factor of 5. The same equation shows that a strong correlation between I_ν and N_d should be expected, as can be seen in Fig. 8. The slope of this correlation decreases for higher values of I_{100} , showing that, for higher temperature, IR intensity increases much faster than the dust column density.

3.2 Dust mass (M_d) and its uncertainty

We estimate an initial value for the dust mass by spatially integrating the dust mass column densities, and obtain $M_d = (1.8 \pm 0.2) \times 10^4 \text{ M}_\odot$. Our estimate is slightly higher than that derived by Schwering (1988), $M_d = (1.4 \pm 0.2) \times 10^4 \text{ M}_\odot$, most of the difference being due to the wider temperature range present in our higher resolution data. The slightly different area used for the integration of dust column density may also contribute.

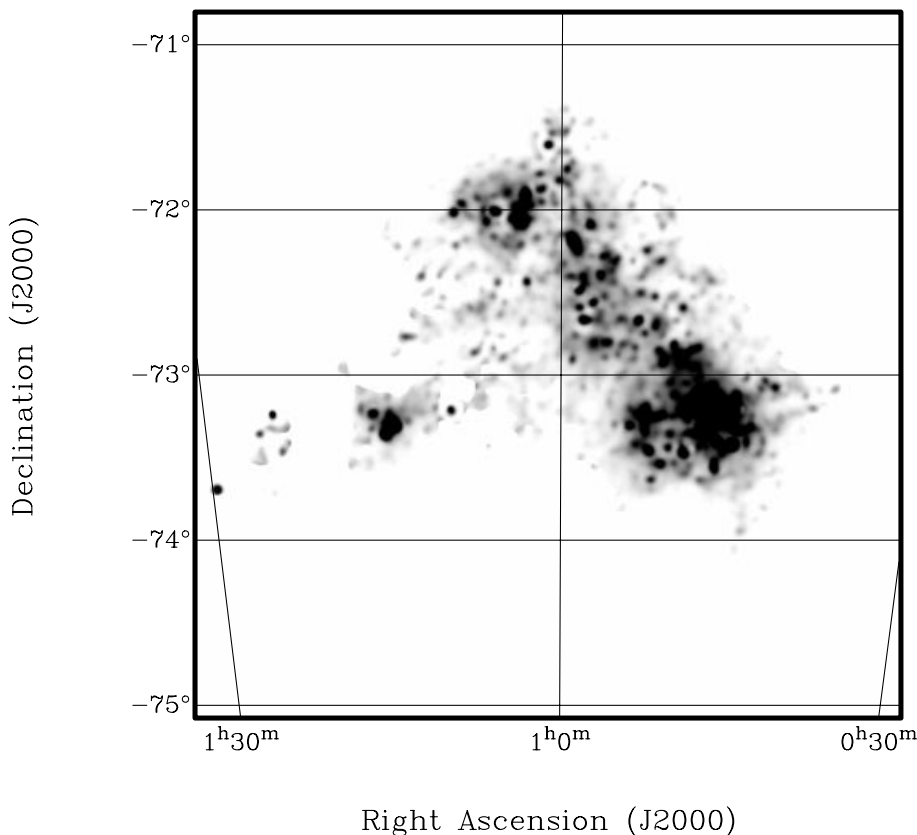


Figure 7. The dust mass column density image of the SMC. The grey-scale range is 0 to $7 \times 10^7 \text{ M}_\odot \text{ sr}^{-1}$ with a linear transfer function. The maximum column density is $2.1 \times 10^8 \text{ M}_\odot \text{ sr}^{-1}$. The conversion factor from $\text{M}_\odot \text{ sr}^{-1}$ to dust particles cm^{-2} is 4.45. The image has a resolution of 1.7 arcmin. A J2000 coordinate grid is overlaid.

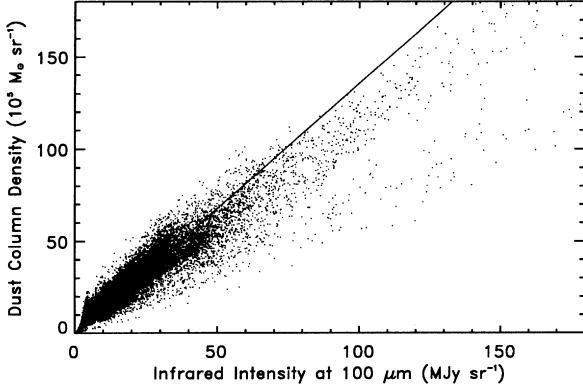


Figure 8. A pixel-to-pixel comparison of the IR intensity at $100\ \mu\text{m}$ (I_{100}) and the dust column density (M_d), showing a strong correlation. The slope decreases for higher values of I_{100} due to the temperature effect. The linear data fit is overlaid.

Although dust grains emit within a narrow temperature range, a line of sight can pass through regions with a different ISRF and therefore with different dust temperature components. Hence, for an object with a large line-of-sight depth, the assumption of a single dust temperature along each line of sight might be a crude approximation. This is the main uncertainty in the derived dust mass (M_d) (Draine 1990). To estimate how big the effect can be, we compare the data with a simple dust model from Schlegel et al. (1998).

If a region in the SMC contains an amount (M_{23}) of dust at temperature 23 K, plus a mass fraction f_T of dust at temperature T , IR intensities corresponding to these two temperature components are given by

$$I_\nu^{23} = \frac{M_{23}}{\alpha_\nu e^{h\nu/23k}} \quad (6)$$

$$I_\nu^T = \frac{M_T}{\alpha_\nu e^{h\nu/kT}}, \quad (7)$$

where $\alpha_\nu = c^2/\kappa_\nu 2h\nu^3$. The measured IR intensity is then equal to a sum of both intensity components: $I_{\text{tot}}(\nu) = I_\nu^{23K} + I_\nu^T$.

Under the assumption of a single dust temperature along a line of sight, $I_{\text{tot}}(\nu)$ for both 60 and $100\ \mu\text{m}$ is used in equation (3) to estimate the dust temperature T' , which will have a value between 23 K and T . This provides a further estimate of the dust column density and dust mass M_d' in the region, which is always less than the true dust mass.

However, if we consider both temperature components present, the dust mass is simply

$$M_d = M_{23} + \frac{f_T}{(1-f_T)} M_{23}. \quad (8)$$

The ratio of recovered (M_d') to true dust mass (M_d) is then given by

$$R(f, T) = \frac{M_d'(f_T, T)}{M_d(f_T)} \quad (9)$$

and is a two-dimensional function of f_T and T , bounded by 1. For a range of mass fractions of the second component, f_T , and a range of temperatures of the second component, T , Fig. 9 shows contours of the ratio of recovered dust mass to true dust mass.

Assuming a single dust temperature model, we have calculated (Section 3) temperatures in the SMC to be in the range 23–45 K,

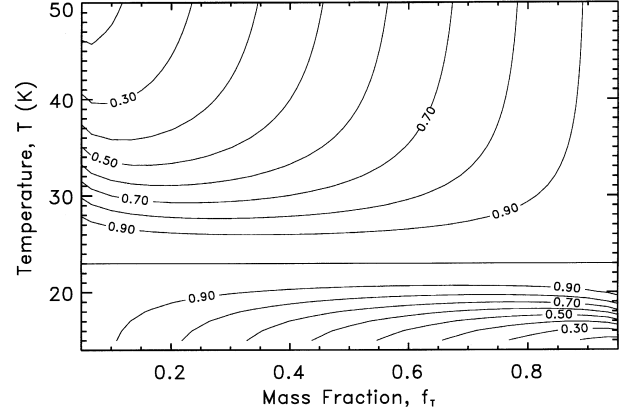


Figure 9. Contours of the ratio of the recovered to true dust mass plotted as a function of temperature and the mass fraction f_T of dust at temperature T . Following Schlegel et al. (1998), this plot illustrates how much the true dust mass can be underestimated if a single temperature is assumed where two temperatures are present (23 K and T).

with the temperature of the diffuse dust component in the range 23–31 K. From Fig. 9, for $19 < T < 30$ K, the true dust mass is underestimated by <30 per cent. Temperatures higher than 31 K (e.g., near H II regions) occur only in a small area of the SMC (~7 per cent) and probably do not contribute significantly to an underestimate of the dust mass.

Another important source of uncertainty in the derived dust mass is cold dust. Because of the quasi-blackbody cooling nature of dust grains, $I_\nu \propto T^{4+n}$, cold dust (<20 K) does not contribute significantly to the IR intensity. Therefore a large amount of cold dust can be masked by the presence of a small amount of cool (~25 K) or warm (~50 K) dust.

The lower limit for dust temperature, contributing to IR emission at $100\ \mu\text{m}$, in the Galaxy is 17 K (Schlegel et al. 1998). For a sample of nearby spiral galaxies, Alton et al. (1998) found that a cold dust component at 18–21 K, and heated by the general ISRF, is prominent at larger radii. Since the SMC has a stronger ISRF than the Galaxy, we would not expect dust in the SMC to be cooler than dust in the Galaxy. Taking 17 K, therefore, as a lower limit for the temperature of cold dust in the SMC, we find from Fig. 9 that the total dust mass would be at most underestimated by 60 per cent. A similar estimate was found in Schwering (1988) using different methods. This provides an estimate of the total dust mass in the SMC, $M_d = 1.8_{-0.2}^{+1.3} \times 10^4 M_\odot$.

4 DUST-TO-GAS MASS RATIO

The comparison of the IR intensity, at all wavelengths from $100\ \mu\text{m}$ to 1 mm, and H I column density in the case of our own Galaxy has shown a good linear correlation for low flux levels (Schlegel et al. 1998; Boulanger et al. 1996), with $I_{100} \approx 0.5W_{\text{H I}} + 0.3$ ($W_{\text{H I}}$ is velocity-integrated H I brightness temperature in units of K km s^{-1}). Substantial scatter has been found for higher flux levels, and has been usually attributed to the presence of molecular hydrogen. In the case of the SMC, Schwering (1988) has noted a good qualitative correlation between the *IRAS* $100\text{-}\mu\text{m}$ intensity and H I column density (using radio data from McGee & Newton 1981), with remarkable differences in some cases (such as N66), where he suggests that gas is either completely blown away or in molecular form. It was also found that $I_{100} \propto N_{\text{H I}}^\beta$, with

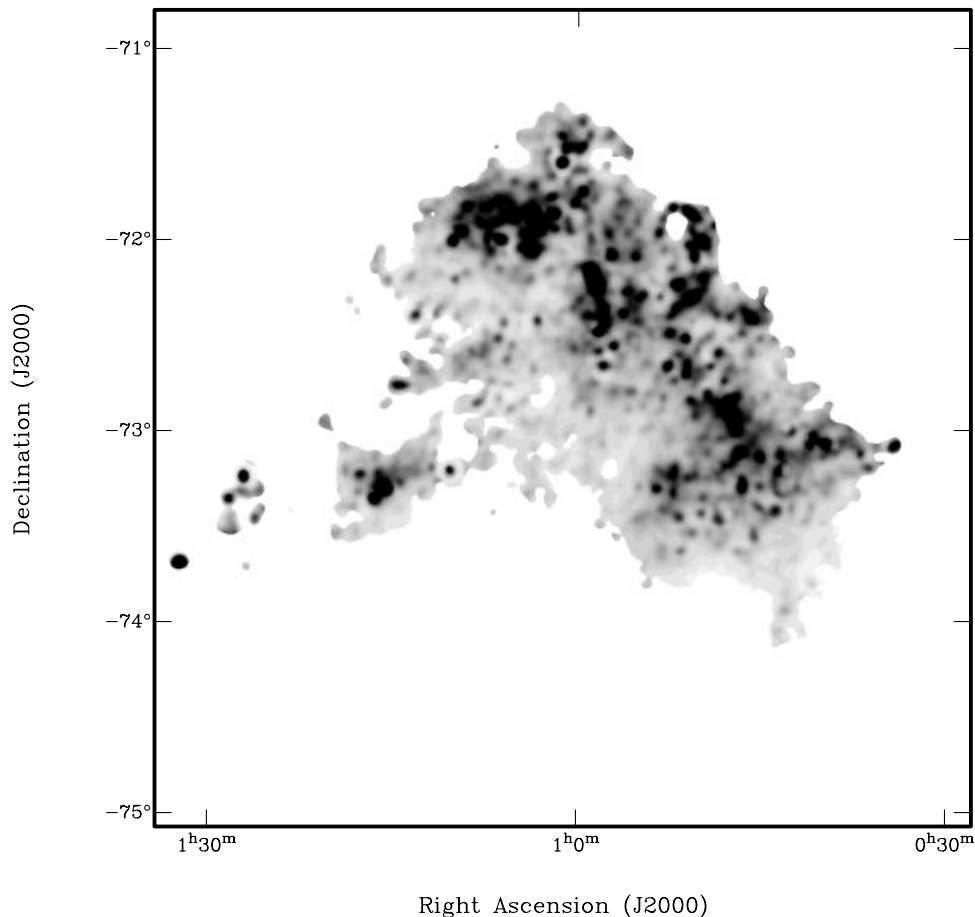


Figure 10. The dust-to-gas mass ratio image of the SMC. The grey-scale range is 0 to 10^{-4} , with a linear transfer function. The maximum dust-to-gas mass ratio of 6×10^{-4} corresponds to N88 and is at position RA $01^{\text{h}}24^{\text{m}}3^{\text{s}}$, Dec. $-73^{\circ}13'45''$ (J2000).

$\beta = 2.2$, showing that IR intensity increases with the H I column density much faster in the SMC than in the Galaxy. The HIRAS data at $100 \mu\text{m}$ and the H I column density, used here, show similar results: a tight correlation between I_{100} and $N_{\text{H I}}$ is seen within the optical bar and the central part of the Eastern Wing, while in the Eastern Wing in general, and especially in the region between the optical bar and the Wing, the correlation is much weaker.

To compare the H I column density with the dust mass column density, we first apply corrections for self-absorption to the H I data (Stanimirovic et al. 1999) and obtain the total H I column density. The dimensionless dust-to-gas mass ratio, derived by dividing dust and H I (mass) column density images (D_{g}), is shown in Fig. 10. The image has a range between 0 and 6×10^{-4} , showing that the gas content (by mass) in the SMC is much higher than the dust content. A significant variation of D_{g} is visible across the SMC, with a variety of small-scale features. The main impression the dust-to-gas ratio image leaves is a ‘granulated’ appearance revealing various H II regions with a significantly higher dust-to-gas mass ratio relative to the spatially averaged value across the whole SMC of 2.5×10^{-5} . It is believed that the gas and dust are well mixed in the ISM (Cox & Mezger 1989). The local variation of the dust-to-gas ratio therefore may reflect more local phenomena, such as:

- (i) an atomic gas deficiency due to H_2 formation;
- (ii) excess dust created in regions of massive star formation, and
- (iii) the presence of cold dust not emitting at $100 \mu\text{m}$.

Similar variation of D_{g} in the SMC has been noted in Schwing (1988) (with a peak of 1.5×10^{-4}), who has attributed most of it to the presence of a significant amount of molecular gas [i.e., (i)]. We address this question in Section 4.2. In Fig. 11 we show the dust-to-gas mass ratio integrated along the optical major axis and plotted as a function of distance from the optical bar. This profile, together with Fig. 10, distinguishes a few regions with a significantly different values of D_{g} .

4.1 D_{g} in discrete H II regions

The highest values of the dust-to-gas ratio are found in discrete bright H II regions (e.g., N81 and N88). H II regions as, in general, sites of the most recent star formation are usually located on the edges or embedded in the clouds of dense and cold gas (Gordon 1988). The brightest H II regions in the SMC are usually found to be larger and more diffuse than those in the Galaxy (Copetti 1990), and their morphology can be explained by the metallicity effect. Being in such a low-metallicity environment, the size of the CO-emitting core within a molecular cloud, associated with an H II region, shrinks while the photon-dominated region (PDR) simultaneously increases its volume (Israel et al. 1996).

The $100\text{-}\mu\text{m}$ IR emission and also the H I emission, associated with an H II region, come from a dense layer surrounding the H II region (Gordon 1988). These layers are usually dust- and gas-rich with dust temperatures (in the SMC) of 31–45 K. Kurt et al.

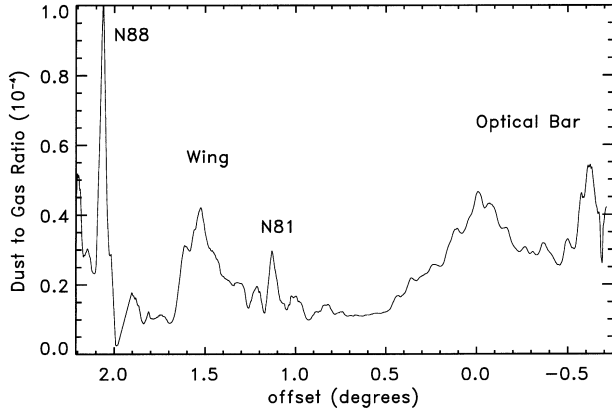


Figure 11. The dust-to-gas mass ratio integrated along the optical major axis (at position angle of 40°) and plotted as a function of distance (in degrees) from RA $00^{\text{h}}52^{\text{m}}$, Dec. $-73^{\circ}00'$ (J2000) along the minor optical axis, starting from south-east. This slice has the same resolution as that in Fig. 6.

(1995) and Kurt & Dufour (1998) examined abundances of C, N and O in a few H II regions in the SMC. They find that, for N88 in particular, the O/H ratio is not indicative of O enrichment arising from mass-loss. This is supportive of case (i) (Section 4) for the excess dust associated with N88. The O/H ratio found for N88 is very similar to values found in a few other H II regions in the SMC. A similar effect has been found in the Galaxy, where Reach, Wall & Odegard (1998) find that most of their excess IR emission from high-latitude clouds comes from dust associated with molecular gas.

4.2 Hidden gas, hidden dust or a real dust-to-gas gradient?

Both the optical bar and the Eastern Wing show in general a similar large-scale trend in D_{g} , peaking in the middle of the region, where most of the recent star formation is concentrated, and having a steep decrease towards the edges (Fig. 11). Diffuse regions in the immediate environment of H II regions have a dust-to-gas ratio very close to the estimated spatial average value (2.5×10^{-5}). Being less exposed to the strong radiation field, their gas content is mostly atomic. Since the IR intensity at 30 K peaks around $100 \mu\text{m}$, the measured dust mass is reasonably well estimated. Therefore the estimated values for the dust-to-gas ratio for these regions are probably accurate.

An interesting feature stands out in Fig. 11. The dust-to-gas ratio drops significantly in the region between the bar and the Eastern Wing. The measured dust temperature here reaches almost the minimum value (23 K). If a significant amount of dust cooler than 23 K is present, an underestimate of the total dust mass could explain the decrease in D_{g} [case (iii) in Section 4]. In the study of a sample of nearby, spiral galaxies, Alton et al. (1998) indeed found that cold dust ($T_{\text{d}} \leq 18\text{--}21$ K) is more prevalent at larger galactic radii.

On the other side, further towards the west from the middle of the bar, the profile in Fig. 11 shows, interestingly, a secondary maximum almost at the edge of the bar. This increase comes mainly from the loop-like feature shown in Fig. 10. This feature is associated with the H I shells: SMC H I-199, SMC H I-202 and SMC H I-170 (see Staveley-Smith et al. 1997) and with the several neighbouring H II regions. Most likely, molecular gas formation [case (i), Section 4] is again responsible for the high value of D_{g} .

Table 2. An estimate of the mass of cold dust having a temperature of 15, 12, 10 or 8 K. Values are derived under assumption that a particular dust temperature (at 15, 12, 10 or 8 K) is entirely responsible for the total luminosity at $240 \mu\text{m}$, obtained from the low-resolution COBE/DIRBE data.

| Temperature (K) | Mass (M_{\odot}) |
|-----------------|----------------------|
| 15 | 2.4×10^4 |
| 12 | 9.5×10^4 |
| 10 | 3.7×10^5 |
| 8 | 2.9×10^6 |

Let us try now to explain the observed variation of D_{g} as a result of local phenomena (i) and (iii) only. We assume first that the real value of the dust-to-gas ratio is around 1.25×10^{-5} in the region between the optical bar and the Eastern Wing, and that all values for $D_{\text{g}} > 1.25 \times 10^{-5}$ come from the atomic gas deficiency due to the presence of significant amount of molecular hydrogen. Measuring the dust and H I mass in the regions of the SMC where $D_{\text{g}} > 1.25 \times 10^{-5}$, we can estimate the mass of the molecular hydrogen which needs to be added so that the dust-to-total gas ratio in the SMC can everywhere have a constant value of 1.25×10^{-5} . The result is that the required mass of molecular hydrogen is about $8.4 \times 10^8 M_{\odot}$, i.e., ~ 2 times that of atomic hydrogen, and almost 30 times the estimated mass of H_2 of $3 \times 10^7 M_{\odot}$ from CO observations (Rubio et al. 1993). The total H_2 mass of the SMC of $(0.75 \pm 0.25) \times 10^8 M_{\odot}$, estimated by Israel (1997), after a re-examination of the CO to H_2 conversion factor, is still more than 10 times lower than the value suggested here. We therefore conclude that the assumption, in which all dust excess comes from the molecular gas, appears to be untenable.

Another alternative for the variation in D_{g} (of almost a factor of 3) is the presence of cold dust, not seen at 60 or $100 \mu\text{m}$. The low-resolution COBE/DIRBE data at 140 and $240 \mu\text{m}$ provide the best available constraint on dust content on temperatures < 20 K. The $240/140 \mu\text{m}$ ratio map is noisy and has low resolution (0.7 deg) but provides evidence for temperatures as low as 15 K, somewhat lower than the HIRAS lower limit of 23 K. If we assume that all of the $240 \mu\text{m}$ luminosity, Fig. 3, arises from dust at 15 K, then the ‘hidden’ cold dust mass is $\sim 2.4 \times 10^4 M_{\odot}$. This is still insufficient to explain the variation in D_{g} . However, at lower temperatures there can be even larger amount of dust present, as shown in Table 2. It is questionable whether such a large amount of cold dust can exist in the SMC. Future observations at submillimetre wavelengths are necessary in order to determine if such dust is present and, if so, what its origin is and what role it plays in the ISM.

However, for the time being, it appears that neither the atomic gas deficiency due to hidden H_2 , nor the presence of hidden cold dust can explain the derived variation of D_{g} . Although a combination of these effects most likely plays an important role, the existence of the third scenario, the intrinsic spatial variation of D_{g} , seems to be very likely. Intrinsic radial gradients in D_{g} have been seen in several nearby spiral galaxies (Viallefond, Goss & Allen 1982; Viallefond & Goss 1986; Walterbos & Schwing

1987; van der Hulst et al. 1988; Issa, McLaren & Wolfendale 1990) and in our own Galaxy (Sodroski et al. 1997). Sodroski et al. (1997) explain a decrease of D_g with increasing Galactocentric distance as being due to a decrease of the stellar efficiency in recycling of the disc material. As dwarf galaxies, in general, have stochastic star formation and chemical evolution, it is usually hard to notice any radial dependence in their D_g (Issa et al. 1990). The significant large-scale trend in D_g in the SMC, from the optical bar to the Eastern Wing (Fig. 11), may suggest a radial gradient of D_g , seen for the first time in a dwarf galaxy.

4.3 The relationship between D_g and metallicity

Dwek (1998) has presented a model for the dynamical and chemical evolution of dust abundances and composition in the ISM of the Galaxy. In this model, the grain life-cycle starts with the grain formation in quiescent stellar outflows and/or explosive eruptions of novae and type II supernovae. Once formed, dust grains get ejected into the ISM where they are further processed under exposure to various processes which influence their abundance and physical properties. While various processes in the ISM are very destructive for dust grains, the grain growth by the accretion process plays a very important role in establishing the dust mass.

The Dwek (1998) model predicts that D_g decreases with the galactocentric radius and that its decrease tightly follows the ISM metallicity, regardless of the star formation history of the ISM. The correlation between D_g and metallicity appears to be a consequence of the fact that the relative efficiency of the grain destruction and grain accretion processes is constant with time. Both the D_g radial dependence and the correlation with metallicity agree well with the observational results for the Galaxy by Sodroski et al. (1997). The variation of D_g in the SMC may also probe metallicity variations and the evolutionary history of the SMC.

Further support to the dust evolutionary model by Dwek (1998) is given by Lisenfeld & Ferrara (1998), who examined the variation of D_g with metallicity in a sample of dwarf galaxies (including the SMC). They found a correlation between oxygen abundance and dust-to-gas mass ratio:

$$12 + \log O/H \propto (0.52 \pm 0.25) \log(M_d/M_{HI}). \quad (10)$$

Their trend of metallicity as a function of D_g is similar to the trend found by Dwek (1998) in a few different Galactic regions, though with a significant offset. This may be due to the stochastic nature of star formation and chemical evolution in dwarf galaxies and their underestimated dust content (Dwek 1998).

We have applied the correlation from Lisenfeld & Ferrara (1998) to the distribution of D_g along the minor optical axis in the SMC, to predict the spatial variation of the oxygen abundances. The profile is plotted in Fig. 12 showing a variation by a factor of 2 along the minor optical axis, which is quite reasonable. Hence, if the suggested relation between the metallicity and D_g holds in the SMC, a variation in metallicity across the SMC by a factor of ~ 2 could completely explain the observed variation in D_g .

To test whether the suggested correlation by Lisenfeld & Ferrara (1998) holds in the case of the SMC, we measured D_g for a few H II regions with known metallicity (from Dufour & Harlow 1977, Pagel, Edmunds & Fosbury 1978 and Kurt & Dufour 1998). The metallicities predicted by the correlation (filled circles) and the values obtained from observations (crosses) are plotted in

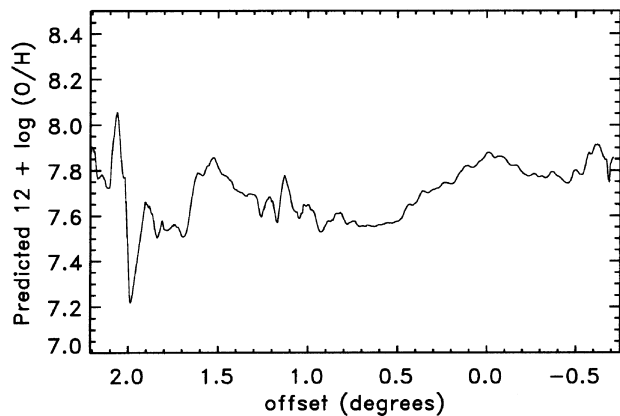


Figure 12. The predicted variation of the oxygen abundance in the SMC for the profile of the dust-to-gas mass ratio shown in Fig. 11 using the correlation found by Lisenfeld & Ferrara (1998). The profile was scaled using the metallicity of H II region N88 from Kurt et al. (1995).

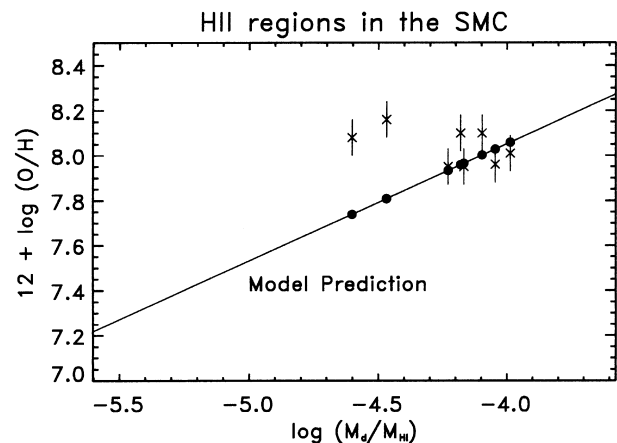


Figure 13. The correlation between the dust-to-gas mass ratio and the oxygen metallicity suggested by Lisenfeld & Ferrara (1998), scaled by the metallicity of H II region N88 from Kurt et al. (1995) and plotted with the solid line. Several H II regions in the SMC, from Dufour & Harlow (1977), Pagel, Edmunds & Fosbury (1978) and Kurt & Dufour (1998), are shown with crosses. Their oxygen metallicities predicted by the correlation are shown with filled circles.

Fig. 13. The model is disappointing in that the current H II metallicity data do not fit the predicted correlation, and may even suggest a negative gradient of the oxygen metallicity as a function of D_g whose physical meaning would be hard to explain. It should be noted, though, that most of these H II regions are situated in the optical bar and have very homogeneous properties. Therefore they may not well represent regions with significantly different value of D_g . Future metallicity measurements of a wider range of objects spread over the SMC are necessary to test the suggested correlation between dust-to-gas ratio and metallicity.

Another important conclusion from the model by Dwek (1998) is that the dust composition (relative abundance of carbon-to-silicate grains) varies with time. As a consequence, several classes of galaxies, with different dust compositions, should be observed. The first class represents young, low-evolved galaxies, where carbon grains are much less abundant than silicate grains. These galaxies have a weak extinction bump at $\sim 0.2 \mu\text{m}$. According to its extinction curve and the dust grain abundances (see Sections 2.1.3 and 2.1.4), the SMC may be a typical representative of this

Table 3. Comparison of the average dust-to-gas mass ratio in the SMC with previous work.

| Reference | N_{HI}^*/E_{B-V} (10^{22} atoms cm^{-2} mag $^{-1}$) | M_{HI}^*/E_{B-V} (10^{-2} g cm^{-2} mag $^{-1}$) | $M_{\text{d}}/M_{\text{HI}}^a$ (10^{-5}) | Method |
|-----------------------|---|---|---|--------|
| Bouchet et al. (1985) | 3.7 | 6.2 | 6.1 | (2) |
| Martin et al. (1989) | 4.6 | 7.7 | 7.5 | (2) |
| Lequeux (1989) | 5.0 | 8.4 | 8.1 | (2) |
| Schwering (1988) | – | – | 5.0 | (1) |
| this paper | – | – | 8.2 | (1) |

^a Obtained using equation (11) for method (2).

category. The second class of galaxies has the extinction curve represented with the Galactic extinction curve, while the model also predicts the existence of the intermediate-age systems, with an excess extinction peak around $0.2 \mu\text{m}$, relative to the Galactic one.

4.4 Comparison with previous work

Two methods for determination of the average dust-to-gas ratio are available in the literature:

(1) where the dust mass is determined from measured IR intensities, and the H I mass is determined from 21-cm spectral line observations ($M_{\text{HI}}/M_{\text{d}}$), as used in this paper, and

(2) where the extinction is determined from photometric observations of stars in the SMC (E_{B-V}), and the H I mass (M_{HI}^*) is measured in front of these stars from the profile of the Lyman α interstellar absorption line (M_{HI}^*/E_{B-V}).

The relationship between these quantities $M_{\text{HI}}/M_{\text{d}}$ and M_{HI}^*/E_{B-V} , obtained in these two methods, is given by

$$\frac{M_{\text{HI}}}{M_{\text{d}}} = R \left[\frac{M_{\text{HI}}^*}{E_{B-V}} \frac{m_{\text{d}}}{m_{\text{HI}}} (1.086\pi a^2 Q_V^{\text{ext}}) \right]^{-1}, \quad (11)$$

where $R = A_V/E_{B-V}$ is the ratio between the visual extinction and the colour excess, a is an average size (radius) of dust grains, Q_V^{ext} is the visual extinction efficiency factor, and m_{d} and m_{HI} are masses of an average dust grain and an H I atom, respectively. The conversion strongly depends on parameters R , a and Q_V^{ext} , whose values are poorly known and also vary from galaxy to galaxy. To compare our results for $M_{\text{HI}}/M_{\text{d}}$ with values previously found for M_{HI}^*/E_{B-V} , we have assumed values: $R = 2.72 \pm 0.18$ (Bouchet et al. 1985), $a = 1 \times 10^{-7}$ m (Schwering 1988) and $m_{\text{d}} = 1.3 \times 10^{-17}$ kg (Schwering 1988). The estimate of Q_V^{ext} is complex, and its value depends on grain nature (size and the refractive index of grain material), geometry and a wavelength. We have assumed here value $Q_V^{\text{ext}} = 1$, estimated for $\lambda = 0.5 \mu\text{m}$ and spherical silicate dust grains having radius of 1×10^{-7} m (from fig. 3.9 in Evans 1994).

In Table 3 we give a comparison of our derived average dust-to-gas ratio with previous estimates. Note that this value was derived from ratio of the total dust mass ($1.8 \times 10^4 M_{\odot}$) to the total H I mass ($2.2 \times 10^8 M_{\odot}$), in a $\sim 2^\circ \times 2^\circ$ area of the SMC and shown in Fig. 10. All estimates of the average dust-to-gas ratio ($M_{\text{d}}/M_{\text{HI}}$) in the SMC are quite close, although the conversion parameters between independent methods (1) and (2) (R , a and Q_V^{ext}) are quite uncertain. The value derived from method (1) in Schwering (1988) is slightly lower than the other ones. The average dust-to-gas ratio derived in this paper is very similar to values obtained by Lequeux (1989) and Martin et al. (1989), although two very different methods were used. The estimated average dust-to-gas ratio in the SMC is almost 30 times lower than in the Galaxy, using an average Galactic dust-to-gas ratio of 1/375 from Schwering (1988).

5 STATISTICAL INVESTIGATION OF DUST AND H I SPATIAL DISTRIBUTION

Instead of describing individual ISM features qualitatively, an alternative way is to view them as having been produced by some random process (Lazarian 1995), and attempt to characterize them with a statistical descriptor. Many statistical descriptors have been used for such a purpose, and some of their advantages and/or disadvantages can be found in Lazarian (1994) and Lazarian & Pogosyan (1997). We use here the 2D spatial power spectra, for both H I and IR data, and the cross spectrum between the two. Although these statistical functions do not provide the complete description of the ISM, they give the hierarchy of scales on which structure is present in the ISM, allowing us, for example, to probe the topology of the ISM and the processes involved in its creation.

5.1 The spatial power spectrum of the IR intensities

We derive here the 2D spatial power spectra of the IR intensity fluctuations at 60 and $100 \mu\text{m}$ (I_{60} and I_{100}). Both images, I_{60} and I_{100} , were for this purpose first Fourier-transformed. We call their Fourier transforms X_{60} and X_{100} , respectively. The average value of the square of the modulus of the transforms, $\langle X_{60} X_{60}^* \rangle$ and $\langle X_{100} X_{100}^* \rangle$, was then measured in 17 annuli of equal width in $\log\sqrt{u^2 + v^2}$ (u and v are the coordinates in the Fourier plane measured in units of λ , and $*$ denotes a complex conjugate of a given function), in the same way as for the H I in Stanimirovic et al. (1999).

The resultant spectra are shown in Fig. 14. Both spectra can be well fitted by a power law, $P(k) \propto k^\gamma$ (where k represents spatial frequencies), over the linear size range ~ 50 pc to ~ 3 kpc, with $\gamma_{60} = -2.4 \pm 0.2$ for the 60- μm band and $\gamma_{100} = -3.2 \pm 0.3$ for the 100- μm band. However, the slopes steepen significantly around 50 pc, resulting in much steeper power spectra for smaller spatial scales. This might suggest that there is not enough IR small-scale structure to contribute to the power spectrum at these spatial scales. However, a significant power may be also missing on larger spatial scales (> 50 pc) because of the quasi-blackbody cooling nature of dust grains, whereby the IR intensity fluctuations will be dominated by warm dust ($T \sim 50$ K), masking the real power of the cool dust ($T \sim 25$ K). From the discussion in Section 4.2, it appears unlikely that such a large amount of cool dust is missing to be able to influence sufficiently the spectrum over a wide range of larger spatial scales (> 50 pc). It is likely, though, that the cool dust may concentrate in small clumps, thereby causing a significant underestimate of power on very small spatial scales, and therefore a change of the power-law slope.

The derived power-law index for the 100- μm band is, nevertheless, similar to the indices found previously for the Galaxy. Gautier et al. (1992) have measured the spatial power

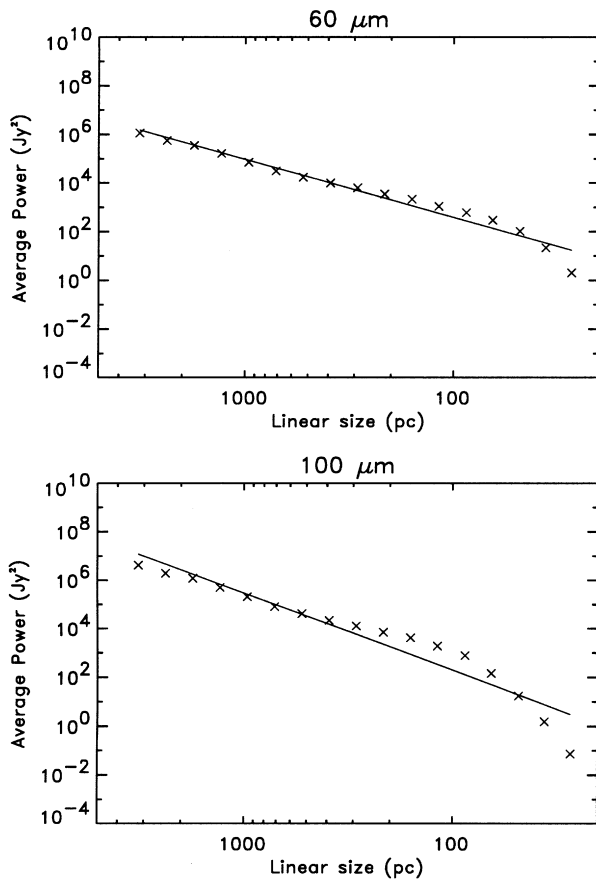


Figure 14. The 2D spatial power spectrum of the 60- and 100- μm intensity images. Linear size L is related to the radius k in the uv -plane by $L(\text{pc}) = d/k(\lambda)$, where $d = 60 \times 10^3 \text{ pc}$ is the distance to the SMC (1 kpc corresponds to 57.3 arcmin and 60λ). Least-squares fits, derived using all data points, are overlaid.

spectrum for a few Galactic cirrus clouds at 100 μm , over the angular scale of 2 arcmin to 8 deg, and found a good power-law fit with an average slope of $\gamma = -3$. Recently, Schlegel et al. (1998) have found a shallower slope of $\gamma = -2.5$ from the full-sky 100- μm maps for angular scales of 1° and over.

We now address the question of radial symmetry of the derived spatial power spectra. In the case when a significant preferred alignment of structure is present, caused by, for example, the tidal stretching or shear, the power spectra will significantly vary for different position angles (azimuth) in the Fourier plane. The azimuthal isotropy of the spatial power spectra has been tested for the Galaxy by Gautier et al. (1992) in the case of dust, and by Green (1994) in the case of HI, and no significant variation has been found. We perform here a similar test for the dust power spectra of the SMC. The same method for measuring a spatial power spectrum was applied on four different segments in the Fourier plane (with position angles 0° – 45° , 45° – 90° , 90° – 135° and 135° – 180° , respectively), performing data averaging in 17 annuli within each segment. The resultant spectra for the 60- μm image are shown in Fig. 15. A possible systematic trend is visible for larger spatial scales. Values for the third and fourth segments seem to be consistently lower than values for the first and second segments. This shows that power spectra for the third and fourth segments have more power on larger spatial scales, which corresponds to an alignment of structure in direction north-east–south-west, i.e.,

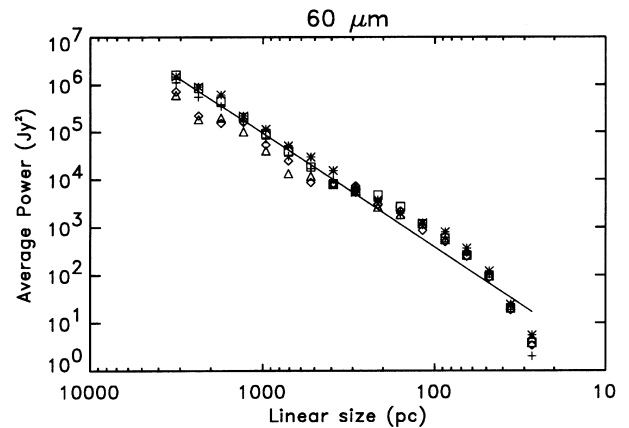


Figure 15. The 2D spatial power spectra of the 60- μm intensity image over the linear size range $\sim 30 \text{ pc}$ to $\sim 3 \text{ kpc}$. To test the azimuthal symmetry of the spatial power spectrum, radial averaging has been performed within four different segments in the Fourier plane: 0° – 45° (asterisk), 45° – 90° (square), 90° – 135° (diamond) and 135° – 180° (triangle). The radially averaged data points within the whole Fourier plane are shown with a plus sign (+) and overlaid with the least-squares fit.

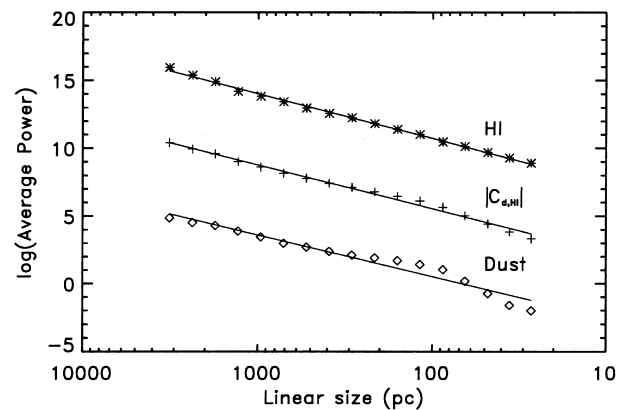


Figure 16. The 2D spatial power spectra of dust and HI mass column densities, labelled as ‘Dust’ and ‘HI’ (in units of M_\odot), together with the spatial amplitude cross spectrum of dust and HI, labelled with $|C_{d,HI}|$ (in units of M_\odot), which will be used in the next section.

along the bar. However, all variations with azimuth seem to be small and within the estimated uncertainties, suggesting that derived spectra can be assumed to be radially symmetric.

5.2 Spatial power spectrum of HI and dust column densities

We turn now to the 2D spatial power spectra of the dust and HI column densities. Both dust (N_d) and HI (N_{HI}) mass column density images were first Fourier-transformed (X_d and X_{HI} are used to denote Fourier transforms of dust and HI, respectively). Assuming the azimuthal isotropy, tested in Section 5.1, the average value of the square of the modulus of the transforms, $\langle X_d X_d^* \rangle$ and $\langle X_{HI} X_{HI}^* \rangle$, was then measured in the usual way. Note that some masking was applied on X_{HI} to exclude four elliptical annuli where the ATCA data were not fully sampled (see Stanimirovic et al. 1999 for more information). Both dust (P_d) and HI (P_{HI}) spatial power spectra are shown in Fig. 16 labelled as ‘Dust’ and ‘HI’.

Both P_d and P_{HI} are well fitted by a power law over a wide

range of spatial scales (30 pc to 3.2 kpc). The power spectrum of the H I column density shows a remarkably tight power-law fit, $P_{\text{H I}}(k) \propto k^{-3.31 \pm 0.01}$. The power spectrum of the dust column density can be fitted with $P_d(k) \propto k^{-3.1 \pm 0.2}$, and is very similar to the spectrum of 100- μm intensity image. This spectrum also shows a slight change of slope on very small spatial scales (< 50 pc). Some deficiency of power on very large spatial scales may also be present, most likely due to the opacity effect and/or a lack of complete sampling on these spatial scales. Nevertheless, slopes for P_d and $P_{\text{H I}}$ appear to be quite similar.

With thinner velocity slices ($\sim 5 \text{ km s}^{-1}$), the result $P_{\text{H I}}(k) \propto k^{-3.05}$ was previously obtained using the same H I data (Stanimirovic et al. 1999). The spatial power spectrum of the H I mass column density (integrated along the whole velocity range, i.e., a ‘thick’ velocity slice) is presented here for the first time. There is a significant change in the power-law index from $\gamma = -3.04 \pm 0.02$ for ‘thin’ velocity slices to $\gamma = -3.31$ for a ‘thick’ velocity slice. The simple explanation is that integration along the velocity axis has washed out some small-scale structure, leaving more power on the larger spatial scales. However, Lazarian & Pogosyan (2000) argue that the slope variation for different velocity slices contains important information about the origin of the spatial power spectrum. They show that ‘thick’ velocity slices represent H I density fluctuations, while ‘thin’ slices show the turbulent velocity fluctuations. The power spectra given by Stanimirovic et al. therefore seem to have a significant velocity contribution.

The slope of P_d agrees well with the predictions by Padoan, Jones & Nordlund (1997), although very different approaches have been performed. In the investigation of the distribution of dust in dark molecular clouds by Lada et al. (1994), the simultaneous determination of colours for hundreds of stars was performed. A plot of the mean visual extinction (A_V) versus its dispersion (σ), $\sigma - A_V$, showed an interesting correlation which appears to have an important role in the study of structure of dark clouds. Padoan et al. (1997) have shown that the $\sigma - A_V$ correlation originates in the strong fluctuations of the 3D density distribution in dark clouds, produced by random supersonic motions. Their numerical simulations of the 3D random density distribution shaped by supersonic flows show a power-law behaviour of the spatial power spectra, $P(k) \propto k^{-2.6 \pm 0.5}$, which is consistent with observations of the cloud IC 5146 by Lada et al. Projected in two dimensions, this results in the 2D density fluctuation spectrum, with the slope between -3.0 and -3.1 (P. Padoan, private communication).

The power-law fit of both dust and H I column density power spectra shows that the hierarchical structure organization is present within dust and H I content of the ISM in the SMC, with no preferred spatial scales for dust and H I clouds. The power-law indices for dust and H I are similar, showing that similar processes are probably involved in the shaping of both dust and H I content of the ISM. One interpretation of the $P(k)$ power-law, as discussed in Stanimirovic et al. (1999), is that the ISM in the SMC has a fractal nature, created by the supersonic turbulence. The mean slope of dust and H I power-law fits, $\langle \gamma \rangle = -3.2 \pm 0.1$, suggests the projected fractal dimension of $D_p = 1.4 \pm 0.1$ (for the relationship between the power spectrum and the projected fractal dimension see Stanimirovic et al. 1999), or the volume fractal dimension of $D = 2.4 \pm 0.1$, assuming a simple relationship $D = D_p + 1$ suggested by Beech (1992). This is very similar to the measured volume fractal dimension for molecular clouds by Elmegreen & Falgarone (1996).

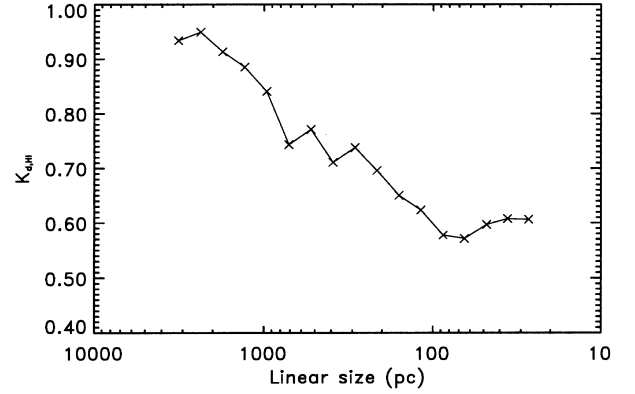


Figure 17. The spatial coherency spectrum of dust and H I mass column densities, $K_{\text{d,H I}}(k)$.

Table 4. A summary of all $P(k) \propto k^\gamma$ slopes derived in this paper.

| | γ |
|--|------------------|
| 60- μm intensity | -2.4 ± 0.2 |
| 100- μm intensity | -3.2 ± 0.3 |
| H I ‘thin’ slices ($\sim 5 \text{ km s}^{-1}$) | -3.04 ± 0.02 |
| N_d , dust column density | -3.1 ± 0.2 |
| H I ‘thick’ slice, H I column density | -3.31 ± 0.01 |
| $ C_{\text{d,H I}} $, cross spectrum | -3.23 ± 0.03 |

5.3 The spatial coherency spectrum

Finally, we investigate the statistical correlation between H I and dust column density using the cross spectrum, $C_{\text{d,H I}} = \langle X_d X_{\text{H I}}^* \rangle$. $C_{\text{d,H I}}$ is a complex function and its amplitude, $|C_{\text{d,H I}}|$ (shown in Fig. 16), was used to derive the spatial coherency spectrum (Yuen & Fraser 1979) presented in Fig. 17:

$$K_{\text{d,H I}}(k) = \frac{|C_{\text{d,H I}}(k)|^2}{P_d(k)P_{\text{H I}}(k)}. \quad (12)$$

Some characteristics of the derived spatial and cross spectra in this paper are summarized in Table 4.

The spatial coherency spectrum is a measure of correlation between two functions on different spatial scales. Its values range between 0 and 1. In the case of two independent processes, $K_{\text{d,H I}}(k) = 0$ for all k , while $K_{\text{d,H I}}(k) = 1$ (for all k) if one process is a linear function of the other one, or both processes are linear functions of some third random process. Fig. 17 shows that, in general, dust and H I are spatially well correlated over a wide range of spatial scales. $K_{\text{d,H I}}$ increases from ~ 0.6 to ~ 1 , for spatial scales from ~ 50 pc to the largest one used here to measure the power spectrum, ~ 3.2 kpc. For very small spatial scales (30–50 pc), which correspond mainly to H II regions, no good correlation is expected because hydrogen here leaks, being either ionized or in molecular form. However, Fig. 17 shows on these scales a small bump in $K_{\text{d,H I}}$. We note that this may be caused by an underestimate of cold dust on these spatial scales, as already discussed.

6 SUMMARY

We have presented here the high angular resolution far-infrared HIRAS images of the SMC, at 12, 25, 60 and 100 μm , for the first

time. These images have angular resolutions of 1 arcmin at 12, 25 and 60- μm , and 1.7 arcmin at 100 μm . The HIRAS data were used in conjunction with a combination of the ATCA and Parkes telescope H I spectral line surveys of the SMC to reach the following conclusions.

(1) The integrated HIRAS spectrum suggests that PAH molecules and VSGs do not play an important role in the SMC. The far-IR part of the spectrum can be reasonably well modelled with a composition of the quasi-blackbody curves for the temperature range 15–30 K, showing that large dust grains in thermal equilibrium are predominantly responsible for IR emission at $\lambda \gtrsim 45 \mu\text{m}$. Assuming the standard dust model, dust temperature and dust column density distributions were derived. Dust temperatures range from 23 to 45 K, which is somewhat warmer than for our Galaxy (17–30 K). While estimating the total mass of cool dust, it was found that the dust mass may be underestimated by <30 per cent due to the presence of different temperature components along the line of sight, and altogether by <60 per cent if the dust cooler than 20 K exists in the SMC. The total amount of cool dust in the SMC is thus $1.8^{+1.3}_{-0.2} \times 10^4 M_{\odot}$.

(2) The average dust-to-gas ratio in the SMC is, by mass, 8.2×10^{-5} (which is a factor of ~ 30 below the Galactic value). The dust-to-gas mass ratio shows a significant spatial variation, decreasing considerably from the optical bar towards Eastern Wing. If interpreted as a deficiency of atomic gas, the mass of molecular hydrogen of $\sim 8 \times 10^8 M_{\odot}$ is required to account for this variation. This is about double the H I mass and about 10–30 times the mass accounted from CO studies. If interpreted as a deficiency of cold dust, a huge amount ($\sim 10^6 M_{\odot}$) must be present at temperatures of 9 K, or below, in order not to be seen by COBE/DIRBE. Although a combination of both deficiencies probably plays an important role, the existence of an intrinsic radial dependence of the dust-to-gas mass ratio, already found in several spiral galaxies, is very likely.

This radial dependence of the dust-to-gas mass ratio could be explained by the recent model for the dynamical and chemical dust evolution in the ISM (Dwek 1998). This model also predicts a tight correlation between the dust-to-gas ratio and metallicity. Using the correlation by Lisensfeld & Ferrara (1998) found from a sample of dwarf galaxies, we predict metallicity variations across the SMC. However, the current observational data for H II regions in the SMC appear to be not consistent with the proposed correlation.

(3) The 2D spatial power spectra of the IR intensity at 60 and 100 μm , H I column density and dust column density, obey the relation, $P(k) \propto k^{\gamma}$. This suggests a hierarchical structure organization, with no preferred sizes for dust and H I clouds. The power-law indices are reasonably similar for H I and dust column densities, with $\langle \gamma \rangle = -3.2$. One interpretation of the $P(k)$ power-law is that the dust and H I content of the ISM in the SMC has a fractal nature, with the volume fractal dimension of $D = 2.4$. This is similar to values obtained by other authors for molecular clouds in the Galaxy, and may imply similar mechanisms for structure formation.

(4) The spatial coherency spectrum shows that dust and H I are well correlated for spatial scales larger than 50 pc, with the correlation coefficient ranging between 0.6 and 1.

The high-resolution IRAS data of the SMC at 12, 25, 60 and 100 μm , as well as the H I and dust column density images, are available electronically from the ATNF SMC web page (see http://www.atnf.csiro.au/research/smc_h1/).

ACKNOWLEDGMENTS

We thank Jeroen van Hoof and Willem Vermin of the SARA computing centre in Amsterdam for their support and advice on the use of their computing equipment, as well as Walter Hoffman and Dick van Albada of the Computational Science institute. We are grateful to Jim Caswell, Raymond Haynes and an anonymous referee for their beneficial comments on this paper. We thank K. Brooks, B. K orbalski, J. Dickey, R. Ekers, A. Lazarian and P. Padoan for stimulating and fruitful discussions. We appreciate Mark Calabretta's help with COBE/DIRBE data. We acknowledge use of the KARMA visualization software for some figures (Gooch 1995). SS also acknowledges the Kapteyn Astronomical Institute and Laboratorium voor Ruimteonderzoek, SRON, for their kind hospitality during one part of data analyses, and the University of Western Sydney Nepean for travel support. TjRB acknowledges financial support provided by the Netherlands Organization for Scientific Research (NWO) through its Massive Parallel Computing (MPR) program.

REFERENCES

- Alton P. B. et al., 1998, A&A, 335, 807
 Assendorp R., Bontekoe T. R., de Jonge A. R. W., Kester D. J. M., Roelfsema P. R., Wesselius P. R., 1995, A&AS, 110, 395
 Aumann H. H., Fowler J. W., Melnyk M., 1990, AJ, 99, 1674
 Beech M., 1992, Ap&SS, 192, 103
 Beichman C. A., Neugebauer G., Habing H. J., Clegg P. E., Chester T. J., 1985, Infrared Astronomical Satellite Catalogs and Atlases. Explanatory Supplement. Jet Propulsion Lab., California Inst. of Tech., Pasadena, p. VII-1, VI-27
 Bontekoe Tj. R., Koper E., Kester D. J. M., 1994, A&A, 284, 1037
 Bouchet P., Lequeux J., Maurice E., Pr evot L., Pr evot-Burnichon M. L., 1985, A&A, 149, 330
 Boulanger F., Abergel A., Bernard J.-P., Burton W. B., Desert F.-X., Hartmann D., Lagache G., Puget J.-L., 1996, A&A, 312, 256
 Cao Y., Terebey S., Prince T. A., Beichman C., 1997, ApJS, 111, 387
 Copetti M. V. F., 1990, A&A, 229, 533
 Cox P., Mezger P. G., 1989, A&AR, 1, 49
 Davies R. D., Elliot K. H., Meaburn J., 1976, Mem. R. Astron. Soc., 81, 89
 de Vaucouleurs G., de Vaucouleurs A., Corwin H. G., Buta R. J., Paturel G., Fouqu e P., 1991, Third reference Catalogue of Bright Galaxies. Springer-Verlag, New York (RC3)
 Draine B. T., 1990, in Thronson H. A., Jr., Shull J. M., eds, The Interstellar Medium in Galaxies. Kluwer, Dordrecht, p. 483
 Draine B. T., Anderson N., 1985, ApJ, 292, 494
 Dufour R. J., Harlow W. V., 1977, ApJ, 216, 706
 Dwek E., 1998, ApJ, 501, 643
 Dwek E. et al., 1997, ApJ, 475, 565
 Dyson J. E., Williams D. A., 1997, Physics of the Interstellar Medium. Institute of Physics Publishing, Bristol, England, p. 25
 Elmegreen B. G., Falgarone E., 1996, ApJ, 471, 816
 Evans A., 1994, The Dusty Universe. John Wiley & Sons, Praxis Publishing, Chichester, p. 54
 Gautier T. N., Boulanger F., Perault M., Puget J. L., 1992, AJ, 4, 103, 1313
 Gooch R. E., 1995, in Shaw R. A., Payne H. E., Hayes J. J. E., eds, Astronomical Data Analysis and Software Systems V, ASP Conf. Ser. Vol. 77. Astron. Soc. Pac., San Francisco, p. 144
 Gordon K. D., Clayton G., 1998, ApJ, 500, 816
 Gordon M. A., 1988, in Kellermann K., Verschur G. L., eds, Galactic and Extragalactic Radio Astronomy. Springer-Verlag, New York, p. 37
 Green D. A., 1994, Ap&SS, 216, 201
 Gull S. F., Skilling J., 1991, MEMSYS5 Users Manual. Maximum Entropy Data Consultants Ltd.
 Hauser M. G., Kelsall T., Leisawitz D., Weiland J., 1998, COBE Diffuse

- Infrared Background Experiment (DIRBE) Explanatory Supplement. *COBE* Ref. Pub. No. 98-A (Greenbelt, MD: NASA/GSFC), available in electronic form from NSSDC, p. 113
- IRAS* Point Source Catalog, Version 2, 1988, Joint *IRAS* Science Working Group, U.S. Government Printing Office, Washington D.C.
- Israel F. P., 1997, *A&A*, 328, 471
- Israel F. P., Koornneef J., 1988, *A&A*, 190, 21
- Israel F. P., Maloney P. R., Geis N., Herrmann F., Madden S. C., Poglitsch A., Stacey G. J., 1996, *ApJ*, 465, 738
- Issa M. R., MacLaren I., Wolfendale A. W., 1990, *A&A*, 236, 237
- Kester D. J. M., Bontekoe Tj.R., 1994, in Terebey S., Mazzarella J., eds, *Science with High Spatial Resolution Far-Infrared Data*. JPL Publication 94-5, p. 23
- Knapp G. R., 1990, in Thronson H. A., Shull J. M., eds, *The Interstellar Medium in Galaxies*. Kluwer Academic Publishers, p. 3
- Koornneef J., 1982, *A&A*, 107, 247
- Koornneef J., 1984, in van der Bergh S., de Boer K. S., eds, *Proc IAU Symp. 108, Structure and Evolution of the Magellanic Clouds*. Reidel, Dordrecht, p. 333
- Koornneef J., Israel F. P., 1985, *ApJ*, 291, 156
- Kulkarni S. R., Heiles C., 1988, in Kellermann K., Verschur G. L., eds, *Galactic and Extragalactic Radio Astronomy*. Springer-Verlag, New York, p. 107
- Kurt C. M., Dufour R. J., Garnett D. R., Skillman E. D., Mathis J. S., Peimbert M., Torres-Peimbert S., Walter D. K., 1995, *Rev. Mex. Astron. Astronfis.*, 3, 223K
- Kurt C. M., Dufour R. J., 1998, *Rev. Mex. Astron. Astronfis.*, 7, 202
- Lada C. J., Lada E. A., Clemens D. P., Bally J., 1994, *ApJ*, 429, 694
- Lazarian A., 1994, *Ap&SS*, 216, 207
- Lazarian A., 1995, *A&A*, 293, 507
- Lazarian A., Pogoyan D., 1997, *ApJ*, 491, 200
- Lazarian A., Pogoyan D., 2000, *ApJ*, in press
- Lequeux J., 1989, in de Boer K. S., Spite F., Stasinska G., eds, *Recent Developments of MC Research*. Meudon, France, p. 119
- Li A., Greenberg J. M., 1997, *A&A*, 323, 566
- Lisenfeld U., Ferrara A., 1998, *ApJ*, 496, 145
- Martin N., Maurice E., Lequeux J., 1989, *A&A*, 215, 219
- Mathis J. S., Rimpl W., Nordsieck K. H., 1977, *ApJ*, 217, 425
- McGee R. X., Newton L. M., 1981, *Publ. Astron. Soc. Aust.*, 4, 189
- Murai T., Fujimoto M., 1980, *PASJ*, 32, 581
- Padoan P., Jones B. J., Nordlund A. P., 1997, *ApJ*, 474, 730
- Pagel B. E. J., Edmunds M. G., Fosbury R. A. E., 1978, *MNRAS*, 184, 569
- Putman M. E. et al., 1998, *Nat*, 394, 752
- Reach W. T. et al., 1995, *ApJ*, 451, 188
- Reach W. T., Wall W. F., Odegard N., 1998, *ApJ*, 507, 507
- Rice W., 1993, *AJ*, 105, 67
- Rodrigues C. V., Magalhaes A. M., Coyne G. V., Pirola S. J. V., 1997, *ApJ*, 485, 618
- Rubio M., Lequeux J., Boulanger F., 1993, *A&A*, 271, 9
- Sauvage M., Vigroux L., 1991, in Haynes R. F., Milne D. K., eds, *Proc IAU Symp. 148, The Magellanic Clouds*. Kluwer, Dordrecht, p. 407
- Schlegel D. J., Finkbeiner D. P., Davis M., 1998, *ApJ*, 500, 525
- Schwering P., 1988, PhD thesis, Sterrewacht Leiden
- Schwering P. B. W., Israel F. P., 1989, *A&AS*, 79, 79
- Sivia D. S., 1996, *Data Analysis, a Bayesian Tutorial*. Clarendon Press, Oxford
- Sodroski T. J. et al., 1994, *ApJ*, 428, 638
- Sodroski T. J., Odegard N., Arendt R. G., Dwek E., Weiland J. L., Hauser M. G., Kelsall T., 1997, *ApJ*, 480, 173
- Stanimirovic S., Staveley-Smith L., Dickey J. M., Sault R. J., Snowden S. L., 1999, *MNRAS*, 302, 417
- Staveley-Smith L., Sault R. J., Hatzidimitriou D., Kesteven M. J., McConnell D., 1997, *MNRAS*, 289, 225
- Staveley-Smith L., Kim S., Putman M., Stanimirovic S., 1998, *Rev. Mod. Astron.*, 11, 117
- van der Hulst J. M., Kennicutt R. C., Crane P. C., Rots A. H., 1988, *A&A*, 195, 38
- Viallefond F., Goss W. M., 1986, *A&A*, 154, 357
- Viallefond F., Goss W. M., Allen R. J., 1982, *A&A*, 115, 373
- Walterbos R. A. M., Schwering P. B. W., 1987, *A&A*, 180, 27
- Westerlund B. E., 1991, in Haynes R. F., Milne D. K., eds, *Proc IAU Symp. 148, The Magellanic Clouds*. Kluwer, Dordrecht, p. 15
- Wheelock S. L. et al., 1994, *IRAS Sky Survey Atlas: Explanatory Supplement*. Jet Propulsion Lab., California Inst. of Tech., Pasadena, CA, p. IV-16
- Young E. T., Neugebauer G., Kopan E., Benson R. D., Conrow T. P., Rice W. L., Gregorich D. T., 1985, *A User's Guide to IRAS Pointed Observation Products*. IPAC Report
- Yuen C. K., Fraser D., 1979, *Digital Spectral Analysis*, CSIRO/Pitman, Adelaide, Australia, p. 59
- Zubko V. G., 1999, *ApJ*, 513, L29

This paper has been typeset from a $\text{\TeX}/\text{\LaTeX}$ file prepared by the author.